MACQUARIE University

Determining the self-diffusion coefficient of iron under mantle conditions

Morgan A.W. Stewart Bsc

Department of Earth and Planetary Science

Faculty of Science and Engineering

A thesis submitted in partial fulfillment of the requirements for the degree of Master of Research

Submission Date 09/10/2017

Corrections Submitted 05/12/2017

Corrections Accepted 07/12/2017

Print Date

University of BRISTOL

Supervisors

Simon Clark

Associate Professor - Department of Earth and Planetary Science, Macquarie University

The Australian Centre for Neutron Scattering, Australian Nuclear Science and Technology Organisation

And

Oliver T. Lord

Royal Society research fellow

Department of Earth Sciences, University of Bristol

Statement of originality

This thesis is all original work, submitted as part of the Masters of Research program at Macquarie university, and has not been submitted to any other university or institution. The experimentation and analysis was all my own work, with the exception of the nanoSIMS data collection, which was conducted by Paul Guagliardo at the University of Western Australia, due to time and training constraints.

Morgan Stewart

Table of Contents

Acknowledgements

I would like to acknowledge the Australian Research Council, who have provided me with a research training program scholarship, as well as the Macquarie Planetary Research Centre, which provided funding for my research.

There are a number of people who have helped me over the year, including my wonderful hosts over in Bristol, Diane and Ron, who looked after me while I was sick, and Michael Walter, who brought me dinner, and who I would later find out authored a number of my references. The people over at the University of Western Australia, in particular Paul, Aaron and Matt, who were always helpful even in the face of slowly unfolding disaster. Thanks to Sarath, for the occasional advice and for helping me get EndNote working, Lucas, for helping me out with math, and to Anthony, who read and gave advice on my thesis.

I also want to thank my friends, who helped make the year a bit more bearable. Lastly, thankyou to my parents, without your continued support I could not have completed this degree.

Abstract

Diffusion is one of the key processes that allows material to move around, it is a controlling factor both of planetary formation and of deformation. This study focusses on self-diffusion of fcc phase iron. Here a laser heated diamond anvil cells were used to generate the high pressures and temperatures, simulating mantle conditions. Iron self-diffusion was measured at 43.6 GPa at both 2100 K and 2000 K, giving diffusion coefficient measurements of 1.46×10^{-14} m^2/s^{-1} at 2100 K and 9.92×10^{-14} m^2/s^{-1} at 2000 K.

These diffusion coefficients were then plotted along with existing data at lower pressures against three different diffusion models, to see whether the models include reasonable assumptions and are accurate at predicting the diffusion of iron at high temperatures. All three of the models consistently underestimated the diffusion coefficient at higher pressures by at least two orders of magnitude. One of the models was recalculated using new values for activation volume (1.43 cm^3/mol) and activation energy (431 kJ/mol), the model now reliably predicts the diffusion coefficient of iron at high pressures.

1. Introduction

Diffusion is a key process that allows material to move around in planetary interiors. It is a small-scale process that functions as a rate limiting factor for much larger processes, including the segregation of planets, deformation and plate tectonics (Gordon, 1967). In this thesis the self-diffusion of solid iron is studied under mantle conditions, in order to better the understanding of diffusion rates at high pressures, in an element which plays a key role in the formation of planets.

1.1 Planetary formation

Planets are formed during the early years of a solar system, when the flattened disk of dust surrounding a newborn star is quickly accreting, forming asteroids and comets which combine to form planetesimals (Chambers, 2004; Wood et al., 2006). Planetesimals are formed over thousands of years, and the typical diameter is constrained to be around 10 km (Chambers, 2004; Wood et al., 2006). Due to gravitational interactions and collisions between planetesimals they continue to accrete, growing in size to become proto-planets, similar in scale to the Earth's moon (<5000 km in diameter), within the first million years of a new solar system; on a timescale of tens to hundreds of million years these bodies will combine to form full sized planets (Chambers, 2004; Wood et al., 2006).

At the same time that planets are accreting planetesimals and proto-planets are also undergoing some degree of internal segregation, as these bodies are hot enough and have large enough gravitational forces to begin differentiation, forming metallic cores (Bouhifd et al., 2017; Wood et al., 2006). During the process of planetary formation differentiation occurs as the denser siderophile elements sink to the centre of the planet, forming iron and nickel rich cores (Mann et al., 2009; Wood et al., 2006). This loss of material leaves buoyant lithophile elements to form the mantle and crustal material (Mann et al., 2009; Wood et al., 2006). Importantly, while there are many transportation mechanisms, diffusion is the key process that allows material to be transported and form dense enough concentrations of siderophile elements that they can sink through the proto-mantle (Berg et al., 2017; Mann et al., 2009; Walter and Cottrell, 2013; Wood et al., 2006). There is some discussion as to whether this process occurs in a magma ocean, a partial magma

ocean or in a solid state, each of which would have implications about the rate at which diffusion and differentiation can occur as diffusion is many orders of magnitude faster in liquid than in solids (Bouhifd et al., 2017; Dobson, 2002; Dobson and Wiedenbeck, 2002; Kaminski and Javoy, 2013; Wood et al., 2006). The earliest stages of core segregation may begin under conditions as low as 20 GPa and 2550 K in proto-planets, although it is worth noting that at these conditions iron is a liquid (Kaminski and Javoy, 2013).

The processes controlling the formation of the Earth are far better constrained than the formation of other planets, due to the availability of geophysical, geochemical and isotopic data. The most useful geophysical data for studying the Earth's core is seismology, it is from this data that it is known that the Earth has a liquid outer core, from the presence of a S-wave shadow zone, and solid inner core, based on the conversion of P to S-waves. In addition to this the speed at which seismic waves travel through the core allow for the accurate measurement of the cores density, and from that it's composition (Badro et al., 2014; Deguen, 2012). The composition of the Earth's core is mostly iron, with ~5% nickel, along with small quantities of lighter elements including oxygen, sulphur, silicon and carbon (Allègre et al., 1995; Badro et al., 2014; McDonough and Sun, 1995). Geochemical data on planetary formation comes from the study of meteorites as well as from experiments, the majority of which are conducted in a multi anvil; these studies are used to constrain the behaviour of different elements during differentiation (Bouhifd et al., 2017; Fischer et al., 2017; Righter et al., 2010; Rubie et al., 2011; Rubie et al., 2015; Siebert et al., 2011).

Radioisotope data is useful for studying planetary core formation, in particular the ^{182}Hf-^{182}W system and the $^{235/238}$U-$^{207/206}$Pb system, which act as isotopic clocks for the formation of planetary cores (Wood and Halliday, 2005; Yin et al., 2002). These isotopes can be used to study the differentiation of planets because the parent isotopes and daughter isotopes are partitioned into different reservoirs; for example ^{182}Hf is a lithophile element, and is the parent of ^{182}W, a siderophile element, the same is true in the $^{235/238}$U-$^{207/206}$Pb system (Wood and Halliday, 2005; Yin et al., 2002). By using meteorite data and the ^{182}Hf-^{182}W system the bulk of metal-silicate partitioning in the solar system was constrained to be occurring during the first 30 Myr (Yin et al., 2002). The U-Pb system gives a longer time estimation for core formation of 65-85 Myr, with a secondary stage of accretion as well as the moon forming impact having a substantial impact on the metal partitioning at this time (Wood and Halliday, 2005).

The moon forming giant impact is one of the key stages in the formation of the Earth, as it was the largest impact event; it introduced new material to the proto-Earth, changing its mass and composition, and also provided a lot of heat and energy for mixing (Canup, 2012; Kaminski and Javoy, 2013; Yu and Jacobsen, 2011). The impactor is thought to be a planet with around the same mass as Mars, which collided with the proto-Earth roughly 30 Myr after the Earth began accreting; the giant impact event may have occurred later (>50 Myr), although in this circumstance the Earth must have completed its main stage of accretion by 10 Myr (Yu and Jacobsen, 2011). The result of this impact was the formation of the moon, the loss of material from both planets to space, as well as much of the Mars sized impacting planet's mass being incorporated into the Earth, including a large portion of the impactor's core (Canup, 2012; Ćuk and Stewart, 2012). The giant impact event splits the formation of the Earth into two parts, shown in figure 1.1: the first stage being the early accretion of the Earth, from both differentiated and undifferentiated bodies, and the second being the impact with a Mars sized planet, adding new material, heat and forming the moon (Kaminski and Javoy, 2013).

Although planetary formation has been well studied in recent years, there has been a lack of experimental data at high enough PT conditions to lend weight to the theoretical models. In particular, there has been a lack of studies on planetary formation that take diffusion rates into

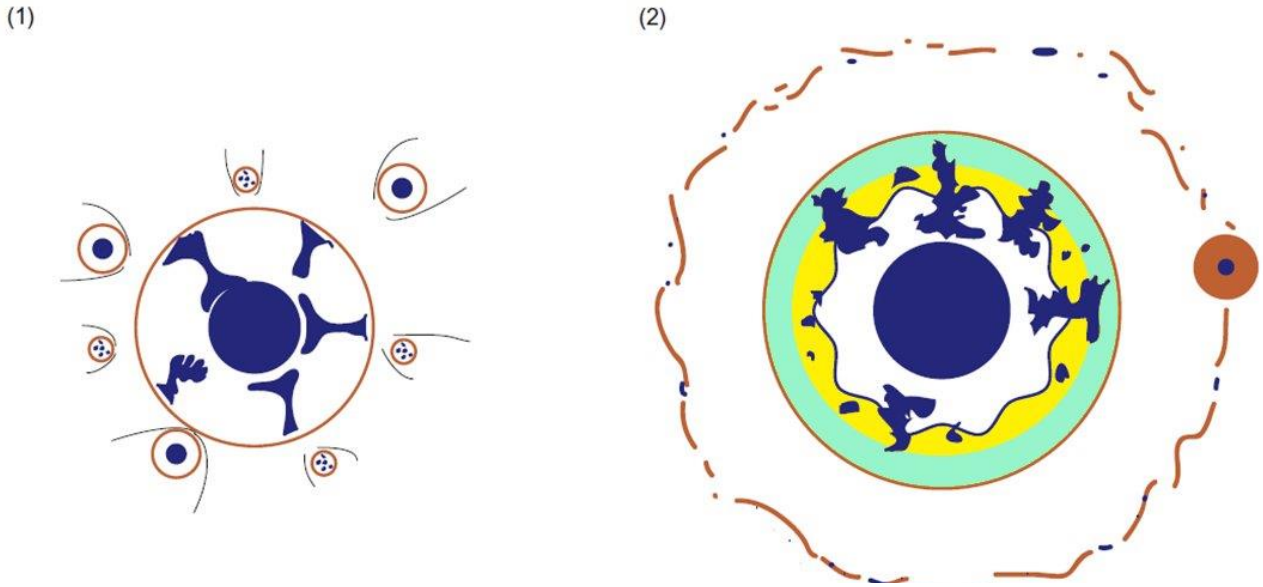

Figure 1.1 is a cartoon of the Earths two main stages of formation. The first stage shows the accretion and differentiation of the proto-Earth, with the lower mantle in white and the core in dark blue. The second stage shows the Earth after the giant impact event, in this model the upper mantle is shown as two parts, yellow (solid) and teal (liquid), the moon is also shown in this image, with a trail of debris which is later incorporated into the moon. This figure is modified from Kaminsky and Javoy, 2013.

account when making their models. In this study experiments are conducted on the diffusion of iron at higher PT conditions than has been studied before. This will help place important constraints on how diffusion impacted the formation of the early Earth and other planetary bodies, as well as how it affects the dynamics of the Earth today.

1.2 Diffusion and deformation

Deformation allows for the movement and rearrangement of crystals, and it is the rearrangement of crystals that powers convection in the solid mantle (Gordon, 1967; Watson and Baxter, 2007). The deformation of solids is one of the driving features controlling the geodynamics of Earth and other planets, and diffusion is one of the main mechanisms for crystal deformation (Gordon, 1967; Watson and Baxter, 2007). When a stress is applied to crystals at high temperatures the atoms will rearrange themselves to lessen that stress, allowing for viscous or plastic behaviour in a solid and deforming the original crystals; this type of deformation is called diffusion creep or *Herring-Nabarro* creep (Gordon, 1967; Watson and Baxter, 2007).

There are three ways in which diffusion creep can occur in minerals, through moving atoms into vacancies, exchanging two or more atoms and through the movement of interstitials, these mechanisms are shown in figure 1.2 (Watson and Baxter, 2007). Vacancies and interstitials are kinds of crystal defects, vacancies being the absence of an atom in a crystal lattice and interstitials being

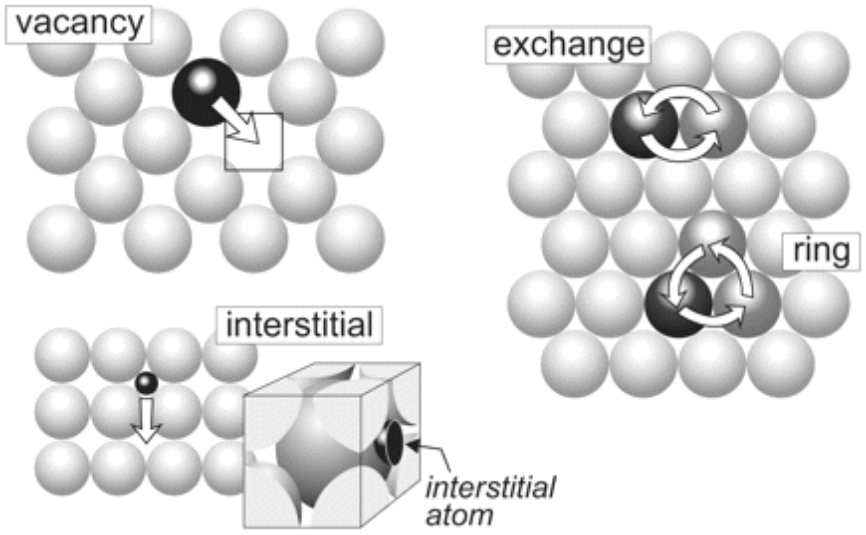

Figure 1.2 is a diagram showing the three ways in which diffusion creep allows atoms to rearrange themselves in a crystal lattice. Top left is vacancy creep diffusion creep, top right is two and three atom exchange diffusion creep and bottom left details the movement of interstitial atoms (Watson and Baxter, 2007).

the presence of additional, smaller atoms. In this study vacancies and exchanges are the diffusion mechanisms which are relevant, as a pure iron system is studied and the presence of diffusing smaller contaminants is not a concern.

1.3 Properties of iron at high pressures and temperatures

There are three crystal structures of iron under high pressure and temperature conditions; the lowest pressure phase is body centred cubic (bcc), the intermediate phase is face centred cubic (fcc) and the high-pressure phase is hexagonal close packed (hcp), figure 1.3 shows the different phase relations (Komabayashi and Fei, 2010). The hcp phase is thought to be what occurs throughout most of the lower mantle and at the core, although new theoretical models predict that a high-pressure bcc phase may become stable at the Earth's core conditions (Belonoshko et al., 2017; Komabayashi and Fei, 2010). There are many different phase diagrams for iron in the literature, each with slightly differing boundaries; the phase diagram in figure 1.3 was modified from several papers in order to be accurate and simple (Anzellini et al., 2013; Dorogokupets et al., 2017; Komabayashi and Fei, 2010; Tateno et al., 2010; Uchida et al., 2001). To achieve this simplicity only

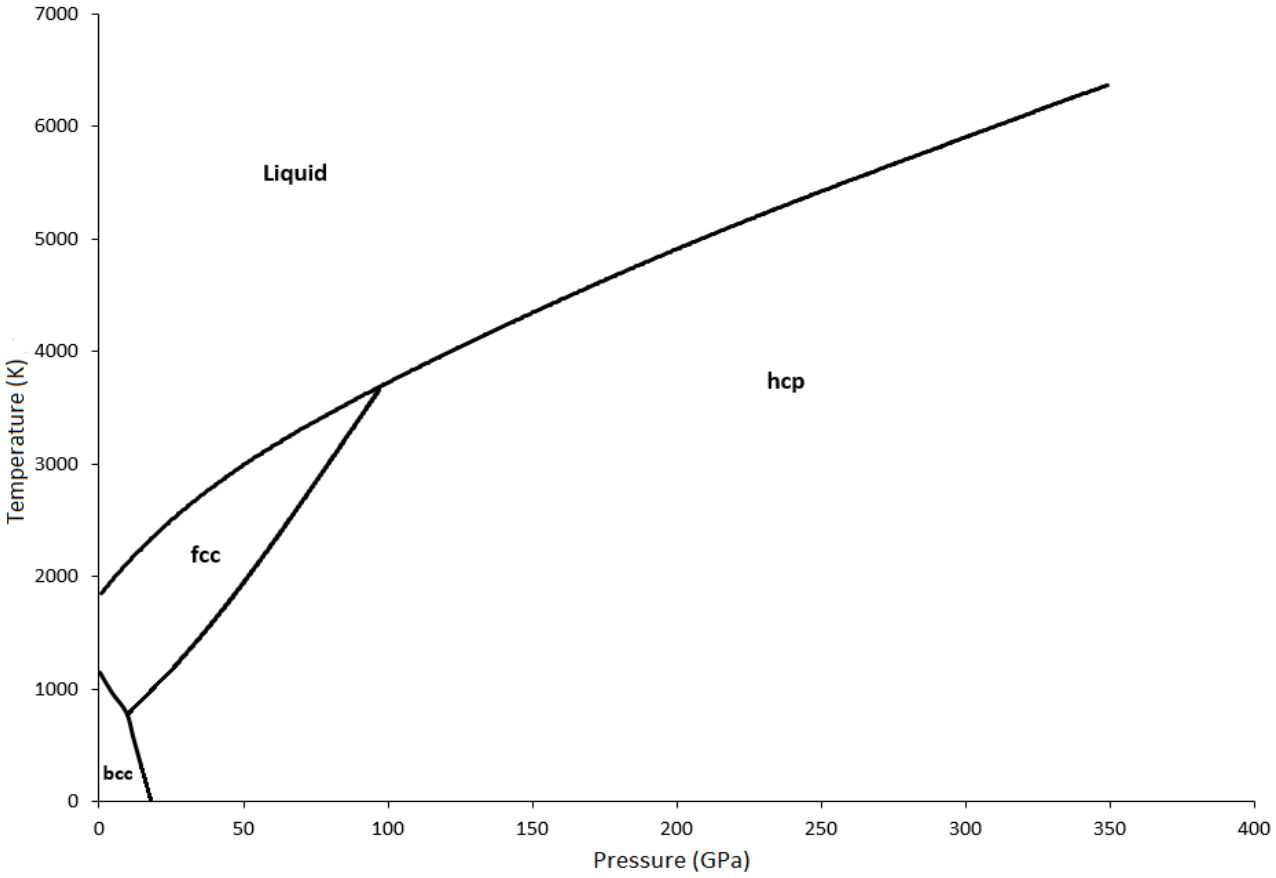

Figure 1.3 Phase relationships of iron. Note that the theoretical high-pressure bcc phase field has been excluded for simplicity (modified from Anzellini *et al.,* 2013: and Komabayashi and Fei, 2010).

the relevant phases for this study have been included, the phases have structurally descriptive labels, bcc, fcc and hcp, rather than the alternative naming system, which uses ε, δ, γ, and α; for accuracy figure 1.3 uses the melting data from Anzellini et al., 2013, and the phase relations from Komabayashi and Fei, 2010.

1.3.1 Current diffusion measurements

There are a number of studies which have investigated the diffusion of iron, most commonly as Fe-Fe diffusion and Fe-Ni diffusion, although there have been studies looking at other systems such as Fe and C diffusion (Dobson and Wiedenbeck, 2002; Goldstein et al., 1965; Heumann and Imm, 1968; James and Leak, 1966). Most of these studies were conducted in the 1960s and 70s at ambient pressure, with very few measurements at higher pressure; the ambient pressure experiments are conducted at temperatures below 1200 K, meaning that many of the samples are ferromagnetic of paramagnetic (Heumann and Imm, 1968; Walter and Peterson, 1969; Yang and Goldstein, 2004; Zhang, 2014).

Due to the absence of iron self-diffusion studies at higher pressures and temperatures this study will compare diffusion rates of iron-nickel diffusion experiments. Iron-nickel diffusion has currently been measured at atmospheric pressure, and at 1, 4, 12 and 23 GPa, the diffusion rates from these studies are listed in table 1.1 (Goldstein et al., 1965; Yunker and Van Orman, 2007). There has also been a single study which uses diamond anvil cells to reach higher pressures, in which Ni was coated onto an FeNi alloy for an experiment run at 65 GPa (Reaman et al., 2012).

1.3.2 Extending measurements to higher pressures

Achieving higher pressures in experiments is restricted by the size of the sample and the equipment used to generate pressure. In general, it is much easier to go to higher pressures on smaller samples, as it requires less overall force to apply pressure on a concentrated area than onto a large area. Previous experiments into Fe-Ni diffusion have used tetrahedral presses, piston cylinders and multi anvils to generate high pressures and temperatures (Goldstein et al., 1965; Yunker and Van Orman, 2007). In the existing piston cylinder experiments the sample assembly was 19mm in length, while the multi anvil assemblies were made using an octahedron with 8 mm

edge lengths, the actual diffusion couples were made using 1mm diameter wires, schematics of these experiments are shown in figure 1.4 (Yunker and Van Orman, 2007).

There are several reasons why multi anvils are not ideal for high pressure studies, even though their relatively large sample size would have makes analysis much simpler. The main reason is that they cannot easily exceed pressures of 25 to 30 GPa, this would severely limit the capabilities of simulating deeper mantle conditions (Yoshino, 2010). There are multi anvils which can go to higher pressures, but they are not commonly in use, the pressure range of these devices are shown in figure 1.5. Another reason is that the furnaces used in multi anvils for high pressure experiments tend to be highly oxidising or reducing environments, depending if a lanthanum chromate or metal foil heater is used, respectively (Ito, 2007). Importantly, very few papers measure the oxygen fugacity, given this thesis will utilise a pure iron experiment oxidation would alter the results, which is why an external heating method such as laser heating is advantageous.

Table 1.1 shows the currently available Fe-Ni diffusion coefficients, along with extrapolated Fe-Fe diffusion data (Goldstein et al., 1965; Reaman et al., 2012; Yunker and Van Orman, 2007). Note that the samples for Goldstein *et al.,* 1965 have been shaded grey, * indicates the sample from Reaman, *et al.,* 2012, which reported diffusion values for Fe and Ni, and not the diffusion values for the various FeNi alloys between these end members.

Pressure GPa	Temperature K	D (m^2/s) 10% Ni	D (m^2/s) 50% Ni	D (m^2/s) 90% Ni	D (m^2/s) Fe-Fe diffusion (extrapolated)
0	1273	4.93E-17	3.94E-16	6.97E-16	3.03E-17
0	1372	3.02E-16	3.50E-15	6.33E-15	1.57E-16
0	1468	2.82E-15	2.50E-14	4.67E-14	1.64E-15
0	1561	1.19E-14	1.05E-13	1.59E-13	7.00E-15
1	1423	1.58E-14	4.50E-14	1.13E-13	2.11E-15
1	1553	2.76E-15	1.09E-14	2.77E-14	7.89E-15
1	1693	6.51E-14	2.31E-13	4.27E-13	3.04E-15
4	1427	1.27E-16	1.21E-15	2.79E-15	7.79E-17
4	1506	6.03E-16	4.12E-15	9.66E-15	4.04E-16
12	1773	1.16E-14	1.98E-14	6.01E-14	4.52E-14
12	1873	9.73E-14	2.98E-13	4.63E-13	4.61E-15
12	1873	1.14E−13	3.16E−13	5.51E−13	3.55E-13
12	1873	5.13E−14	8.46E−14	2.36E−13	2.21E-13
23	1873	6.83E-15	1.35E-14	3.66E-13	3.13E-15
23	1973	3.84E-14	7.97E-14	1.76E-13	3.14E-14
65	2200	1.67E-15*			1.26E-15*
65	2200	6.40E-15*			8.70E-15*
65	1760	3.80E-17*			4.30E-17*

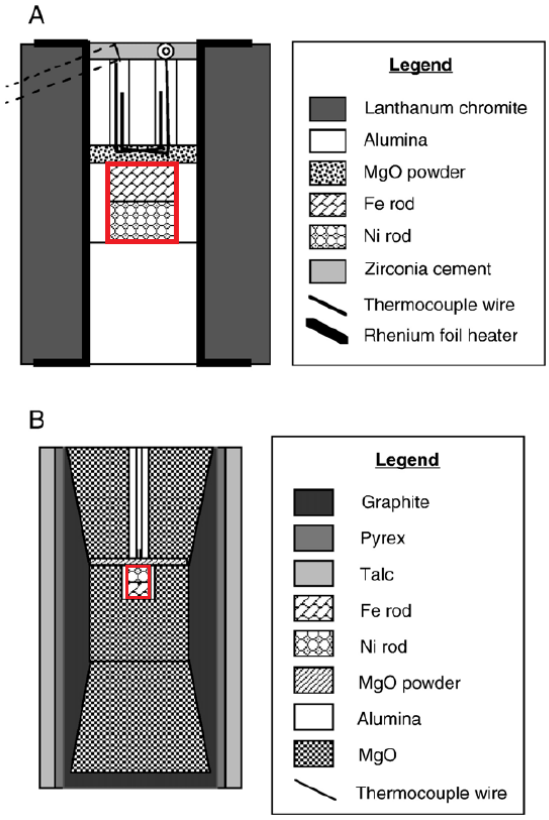

Figure 1.4 shows a multi anvil assembly (A) and a piston cylinder assembly (B), with the samples outlined in red (Yunker and Van Orman, 2007).

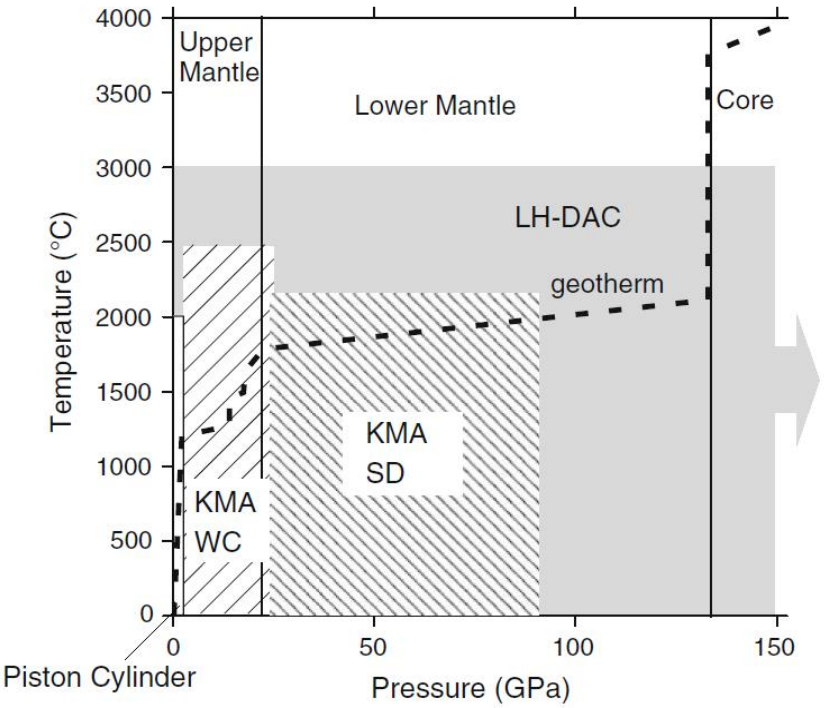

Figure 1.5 a diagram showing the pressure and temperature capabilities of different experiment methods, including piston cylinders, Kawai multi anvils (KMA) in both sintered diamond (SD) and tungsten carbide (WC) varieties, and laser heated diamond anvil cells (LH-DAC). Modified from Toshino, 2010.

In this study, the aim is to extend the existing dataset to higher pressure and temperature conditions by using diamond anvil cells (DACs). DACs are a relatively new technology which was not in common use in the 1960s and 1970s, when the iron self-diffusion and most of the iron nickel diffusion experiments were conducted; a recent study, by Yunker and Van Orman in 2007, increased the pressure to 23 GPa by using multi anvils. The highest pressure phase of iron with existing diffusion data is the fcc phase, and even this phase has only had diffusion measured at relatively low pressures and temperatures. By utilising DACs, it is possible to extend the measurements of fcc iron to much higher PT conditions, and also measure diffusion in the hcp phase of iron for the first time. DACs can achieve much higher pressures than other high-pressure methods because of the size of the samples, which are far smaller; the size of the diamond culet controls how much force is concentrated into one place, smaller culets generate higher pressures however the sample needs to fit into the high-pressure zone. Due to the tiny nature of DAC samples it is possible to do experiments exceeding 100 GPa, however this involves having samples so small that designing such a small experiment and then loading the samples becomes increasingly difficult, analysis after the experiment is also much more challenging and requires more precise equipment (Konôpková et al., 2016).

1.3 Justification for studying iron self-diffusion

There are several reasons for studying iron self-diffusion, it is the most abundant element in the Earth's core and plays an important part in the differentiation of planets, and by studying self-diffusion a number of the problems which affect inter-diffusion experiments are avoided. One of the problems with studying iron-nickel diffusion is that the molar volumes of iron and nickel are similar, but not identical, therefore either a correction for this needs to be made or an assumption that they are the same be maintained (Yunker and Van Orman, 2007). These problems will be even more apparent in other systems, for in an iron-silicon diffusion experiment, where the volume difference between iron and silicon are much greater. Another problem with diffusion experiments involving different elements is that having different concentrations of elements within an alloy will affect the stability field of different phases, for example increasing the nickel content in iron from 5% to 15% will stabilise the fcc field of iron down to lower temperatures and higher pressures (Mao et al., 2006). Conducting iron self-diffusion experiments also has the advantage of having less crystal

defects compared to systems with multiple elements, which should improve the accuracy of the experiments.

1.4 Evaluating the equations used to calculate diffusivity

One of the major goals of this study is to come up with a formula which can be used to accurately predict the diffusion rate of metal at any given pressure and temperature within a certain phase. A useful application of such a formula would be predicting the diffusion rate of any given metal at any point along the Earth's geotherm, or any other planetary body's geotherm.

There are several existing formulas which can be used to calculate the diffusion coefficient *D,* the first equation discussed in this study is from Sammis and Smith, 1981. It describes *D* as a function of D_o, which is a constant derived from diffusion measurements, the activation energy *E**, the activation volume *V**, the universal gas constant *R,* pressure *p* and temperature *T* (Sammis et al., 1981).

(1) $$D = D_0 \exp(\frac{-(E+pV)}{RT})$$

Also from the Sammis and Smith, 1981 paper there is a formula relating the diffusion rate to the melting point of the material T_m and *g*, a function of the activation energy over the melting temperature. In this equation, the pressure component is taken into account with the melting temperature, as increasing the pressure increases the melting temperature.

(2) $$D = D_0 \exp(\frac{-g*T_m(p)}{RT})$$

Yunker and Van Orman, 2007 use a modified version of equation 2, the value 20.4 is $\frac{g}{R}$ which they calculated using their data, D_0 is assigned a constant value of 2.7×10^{-4} m^2/s, see equation 3. The constant D_0 value was assigned due to an apparent absence of a pressure trend when their data was normalised to a constant $\frac{T_m}{T}$ value, given that this study will go to higher pressures, it will be discussed is whether a pressure trend emerges or not.

(3) $$\frac{g}{R} = 20.4$$

then, $$D = 0.00027 \exp(\frac{-20.4*T_m(p)}{T})$$

This equation was made using data from Fe-Ni diffusion experiments up to a pressure of 23 GPa, and given the relatively low PT conditions under which these experiments were conducted it will be one of the goals of this thesis to determine if Yunker and Van Orman's values still work at higher pressures and temperatures. A major issue with this equation is that there is only a melting curve for Fe-Ni alloys at atmospheric pressure, and no values for higher pressures; the T_m values will work for iron diffusion, but for alloys it is limited by the availability of melting curves (Swartzendruber et al., 1991).

The equation used by Zhang, 2014 can be used to create what is currently the most accurate model for predicting the diffusion rate in iron for any given PT conditions. Zhang does however have an issue in his paper due to his choice of iron phase diagrams and the use of Fe-Ni diffusion experiments for the hcp calculations, when adding nickel to the system stabilises the fcc phase to lower temperatures and higher pressures (Mao et al., 2006; Yunker and Van Orman, 2007; Zhang, 2014). Due to this, the model that fits fcc iron diffusion is actually Zhang's model for hcp iron diffusion; he has mistakenly used fcc phase iron nickel to plot his hcp iron model. To try and resolve this issue it would be necessary to use Zhang's formula to recalculate diffusion in fcc iron using the additional diffusion measurements from this study. Zhang uses a cBΩ model to predict diffusion, with the following components; f is a correlation factor which depends on structure and diffusion mechanism, a is the lattice constant, v is the Debye frequency, k_B is the Boltzmann constant, T is temperature, B is the isothermal bulk modulus, c^{act} is a dimensionless factor (see equation 4 in Zhang, 2014 on how to calculate this) and Ω is the atomic volume per atom.

(4) $$D = f a^2 v \exp\left(\frac{-c^{act}\, B\, \Omega}{k_B T}\right)$$

1.5 Aims

To summarise the sections above, the main aim of this thesis is to measure the diffusion coefficient of iron under high PT conditions for both the fcc and hcp phases of iron, this will be achieved by using laser heated diamond anvil cells. The secondary aim is to determine if any trends emerge in the diffusion coefficients at higher pressures, that were not apparent at lower pressures. Finally, this thesis will evaluate each of the diffusion coefficient models to determine which of them is the most reliable, and provide a better model if none of the existing models can predict the diffusion rate in iron at high pressures and temperatures.

2. Experiment methods

2.1 Diamond anvil cells

2.1.1 Preparation of diamond anvil experiments

Preparation of the diamond anvil cells and the iron samples was done at the high-pressure laboratory at the University of Bristol. For most of the samples the diamond anvil cell which had pre-mounted diamonds with a culet diameter of 250 µm was used. These diamonds were cleaned using abrasive strips of silicon and corundum and then wiped with cotton buds and acetone to remove any dirt.

A gasket was then loaded onto the culet of one half of the DAC, with clay supports around the edges, the DAC was then closed and pressurised by hand to make a slight indent on the gasket. Into this small depression, a ruby grain was placed so that the pressure could be measured. The DAC was then closed and pressurised up to 20 GPa to indent the gasket, the pressure was measured using the fluorescence of rubies under a laser, where the wavelength of fluorescing light corresponds to increasing pressure.

The DAC was then depressurised, and an 80 µm hole was cut into the gasket using a laser (a repurposed MicroProbe II). The oxides from cutting were then loosened using a pin and then removed in an ultrasonic bath. The diamonds were then cleaned again in preparation for the KCl discs which insulate the samples. After this the gasket was loaded back on to one half of the DAC.

The KCl discs were prepared by placing powdered KCl onto pistons which were then formed with a hydraulic press into sheets with a thickness of approximately 10 µm. These sheets were then cut into 80 µm discs to fit into the hole cut into the gasket. One disc of KCl was then placed onto the tip of one diamond, while another was placed into the sample chamber of the gasket, this stage of the assembly, before the DAC is closed, can be seen in figure 2.1.

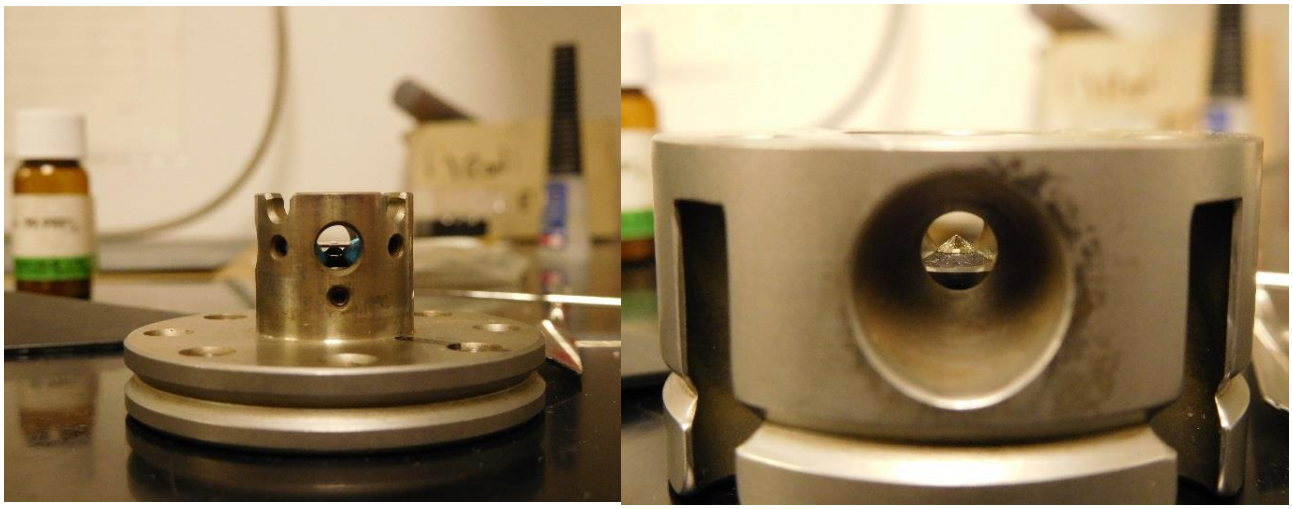

Figure 2.1: the two halves of the DAC, the image on the left shows the gasket in place on the inner half of the DAC.

The sample was then placed into the gasket and the DAC was carefully closed while making sure the alignment was good. The two halves of the DAC were then pushed together by hand to pressurise the sample; the sample was then opened again, excess KCl was removed, and a ruby placed into the sample chamber. At this stage, the DACs are ready for dehydration, which is essential to remove any moisture which the KCl sheets may have absorbed. This process involves closing the DAC with a spacer roughly 2mm high, so that the diamonds do not touch, balsa wood was used as the spacer in these experiments, as it can be easily crushed and does not need to be removed; during this step, the screws of the DAC are only slightly engaged. The DAC is then placed into a ring heated chamber with an argon atmosphere, where it is kept between 126-138 ^{o}C for one hour; once the sample has undergone dehydration the screws of the DAC are then partially engaged and the DAC is removed from the heating chamber.

Once the DAC has cooled it can then be pressurised to the desired experimental conditions; the pressure needs to be measured periodically using ruby fluorescence to make sure that the pressure has not been exceeded and to record the pressure at which the experiment is to take place.

Note that the same procedure was also used to load a different DAC, which was mounted with diamonds that had a 200 µm culet diameter. The sample chamber for experiments prepared in this DAC was 80 µm in diameter, and the KCl discs were also 80 µm.

2.1.2 Experiment assembly

The experiment design is simple, the sample is sandwiched between two discs of KCl, with a ruby grain on one side to measure pressure. This is contained within the hole in a gasket, which is sealed by the two diamonds on either side; figure 2.2 shows a cross section cartoon of how the experiments are assembled.

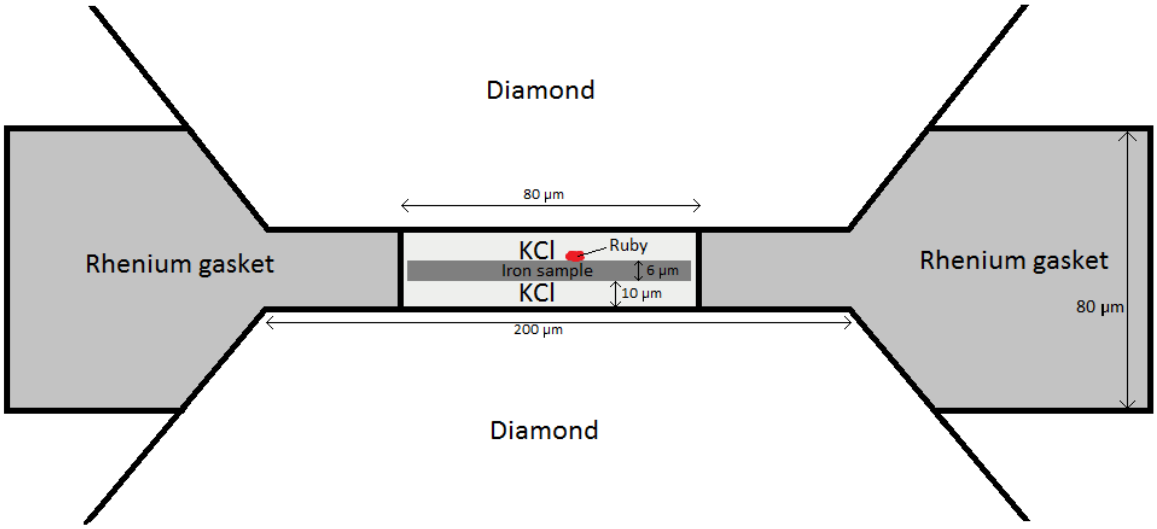

Figure 2.2: a cartoon cross section of the assembly of the experiment. The distance between the diamonds is approximately 26 µm, the sample is 6 µm thick iron foil, with 10 µm of insulating KCl on either side to protect the diamonds. There is a ruby grain within the KCl and the sample assembly is held together by a rhenium gasket.

2.2 Preparation of samples

The samples were prepared by coating a 6 µm thick sheet of iron foil with 95% enriched ^{57}Fe. This was done in a 1 kW SCR Stack and Driver, Model 3AM, which is an evaporation vacuum chamber, shown in figure 2.3. Two test samples were first prepared using 10 mg of Fe loaded into a molybdenum boat, which was mounted on a stand in a way which allowed it to close an electrical circuit, so that the molybdenum becomes a heating element. The target, a thin section slide, was placed with a 9 mm gap between the boat and the slide in the first test, and a 10 mm gap in the second. Due to faulty pressure and power gauges on the aged coating machine, the vacuum chamber was left to pump for 30 minutes in each test. In the first test the sample was heated for 40

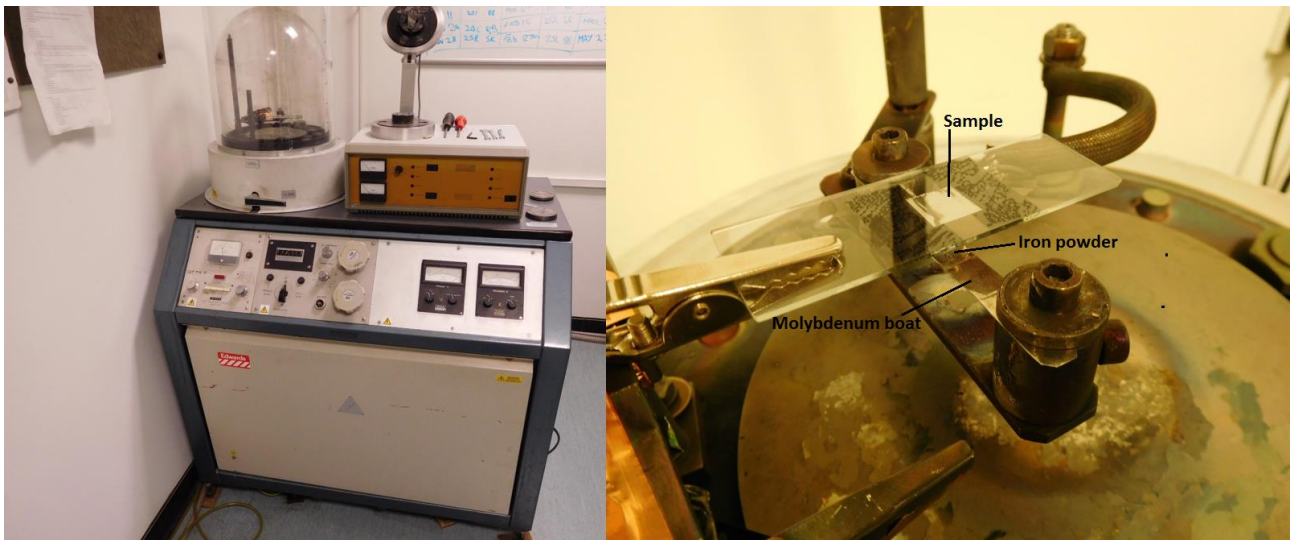

Figure 2.3 shows the vacuum chamber in the left image, and the sample as it is held over the molybdenum boat containing the ^{57}Fe powder before it is evaporated.

seconds, at which it reached a yellow colouration at the greatest temperature, the second test ran for 1 minute and 30 seconds, at which it was held at a yellow hot temperature for 5 seconds. In the first test, only 4.5 mg of material had evaporated, while the second test had evaporated all of the powdered iron.

For the final coating of ^{57}Fe the sample was held at 9 mm above the boat, which contained 9.8 mg of ^{57}Fe, this is shown in figure 2.3; the vacuum was pumped for half an hour and heated for 1 minute, during which it was yellow hot for about 10 seconds.

To gauge how thick the coating of Fe was on each of the slides a Q150T S sputter coater was used to incrementally add more Fe to glass slides and measure the thickness of the layers as they are deposited. The thickness of the iron was then estimated visually by comparing the glass slides with the evaporation test slides. The thickness of the Fe layers on the slides was found to be greater than 70 nm, as at this point the Fe from the sputter coater was still partly transparent, yet the Fe on the test slides was opaque, see figure 2.4.

The samples were then cut into asymmetric discs using the laser cutter, with a diameter of 80 µm for the 250 µm culet diamonds, and 70 µm for the 200 µm culet diamonds; these were then packed between the KCl layers. This shape was improved upon during the experiments, making the cut out both larger and asymmetric; this was to make locating the heating spot easier during analysis, even if the sample was oriented differently, the shape of the samples is shown in figure 2.5.

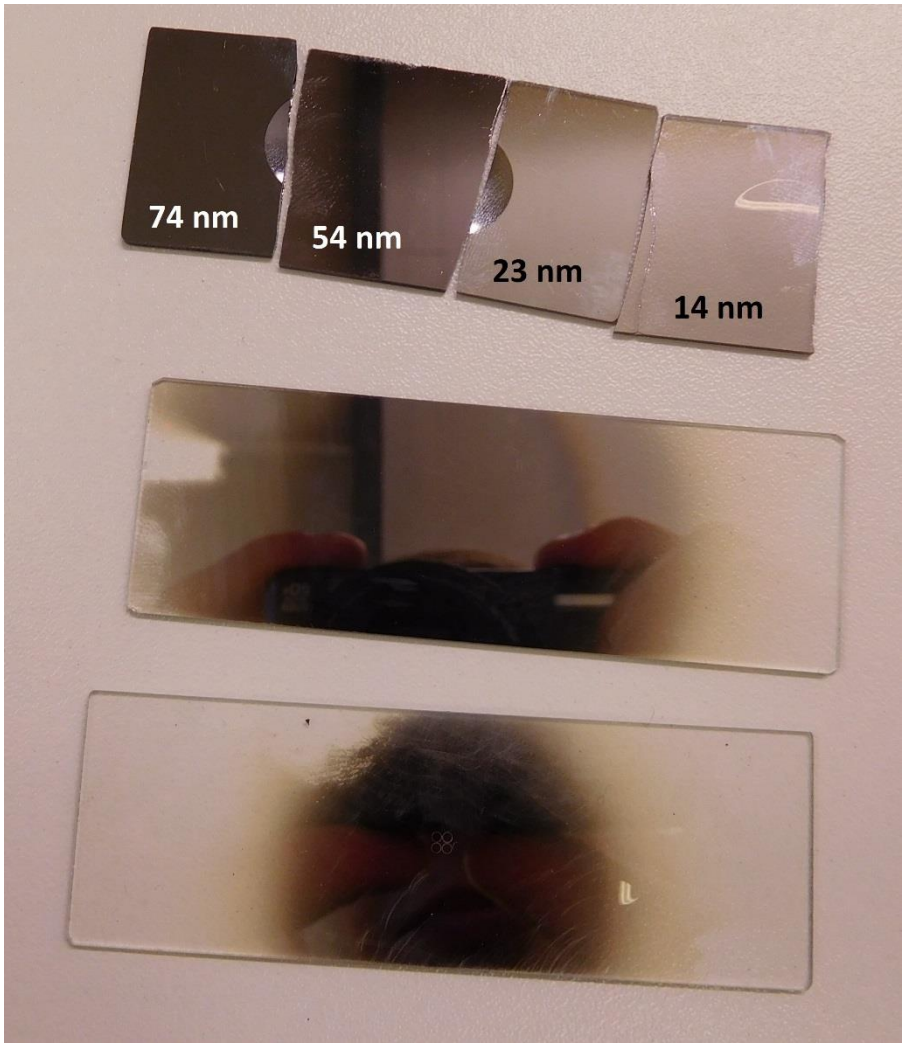

Figure 2.4 shows the test samples used to determine the thickness of the iron layers, the two slides at the bottom have iron concentrated near the centre, becoming dispersed moving away. To create a visual guide for the thickness a sputter coater was used to coat the four pieces of slide at the top of the image, with the thickness in nm being recorded.

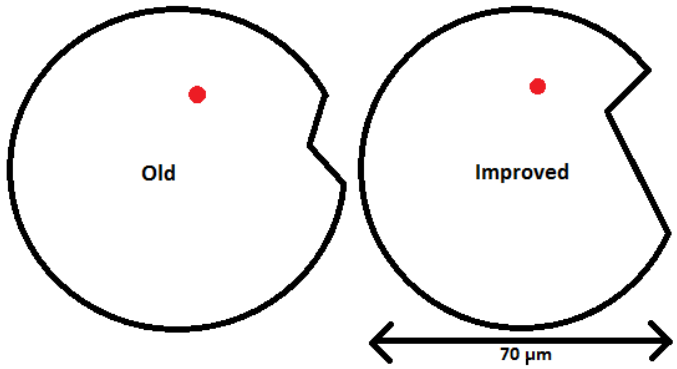

Figure 2.5: a top down view of the shape of the samples, which are discs with portions cut out to aid in identifying laser heating locations., shown here with red dots. With the improved shape there is a better reference point for where the heating site is, and it is also possible to find the laser heating site even if the disc is flipped over. The improved shape was used from sample 3 onwards.

2.3 Experiment conditions

2.3.1 Pressurisation

To pressurise the samples the DAC was slowly tightened, while using ruby fluorescence to monitor the pressure and callipers to measure the screw length; this ensures that the sample pressure can be increased evenly. The peak wavelength of the secondary fluorescence of rubies changes with pressure, and can be used to calculate the pressure of the sample using equation 5; the ruby laser system used to measure the secondary fluorescence is shown in figure 2.6. The pressures and screw lengths for each stage of pressurisation for each sample was recorded, along with the final pressure before and after heating, as the pressure after heating is usually higher.

(5) $$\text{Pressure in GPa} = \frac{1904}{7.665} * \left(\left(\left(1 + \frac{wavelength\ in\ nm - 694.2}{694.2}\right)\right)^{7.665} - 1\right)$$

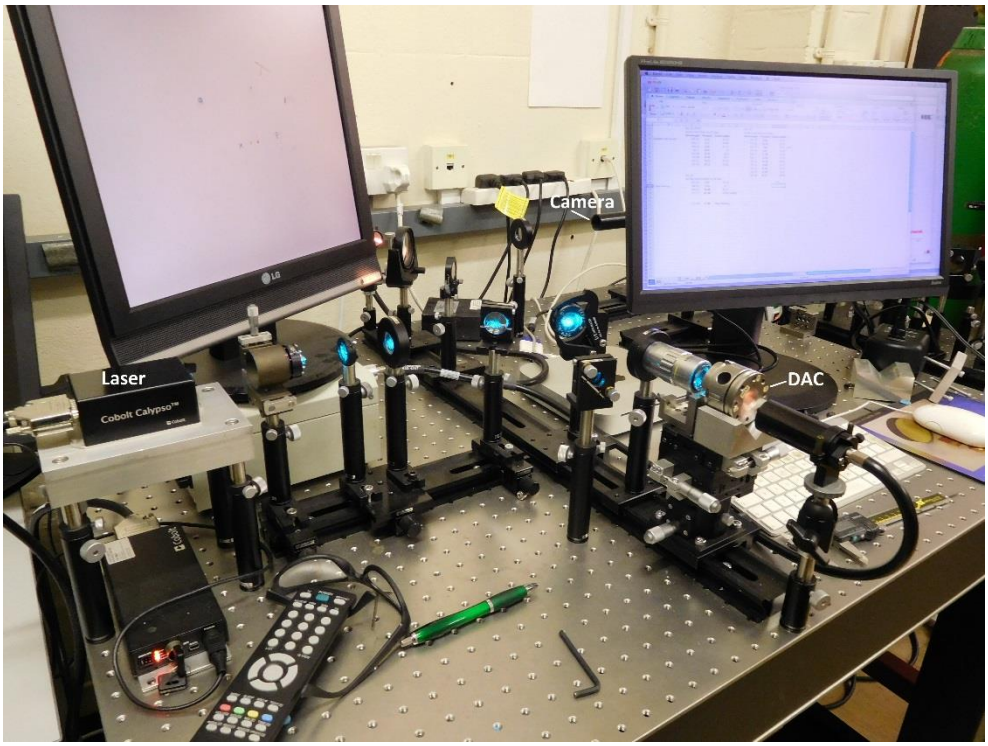

Figure 2.6: the ruby fluorescence laser setup at the University of Bristol.

2.3.2 Heating

The samples were laser heated in the diamond lab at the University of Bristol, this laser heating system consists of two lasers, an Acton SpectraPro 2300i spectrometer and a 4color multispectral imaging radiometry setup, this is shown in figure 2.7, and the 4color is shown in figure 2.8. Before the laser heating system could be used it needed to be recalibrated. This involved aligning the lasers so that they both hit the same point, then aligning the light paths so that they entered the spectrometer and 4color system. Then the spectrometer was calibrated by shining a

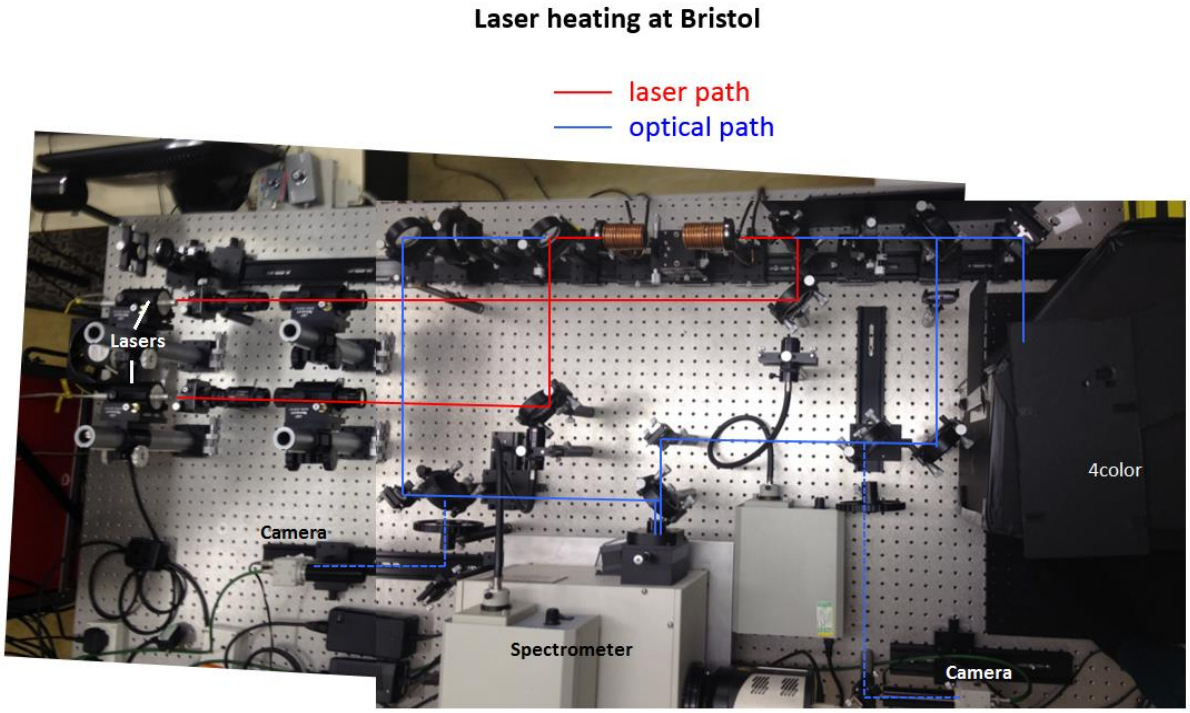

Figure 2.7: an image of the laser heating setup at the University of Bristol. The two lasers go through a system of mirrors and lenses until reaching the sample, the light emitted from the sample then passes through a different set of optics towards the spectrometer, cameras and 4color setup.

white light source with a factory calibrated spectrum through the optics and then comparing and refining the observed spectra based on the factory spectra. The same light was used to calibrate the 4color; this was then used to make the calibration files used in the rest of the experiments.

Once the samples were ready for heating they were mounted in a water-cooled copper block in the centre of the laser pathways. Before the final heating for each sample a test heating spot towards the edge of the sample was used to get the laser power right for the desired heat, this was done by slowly ramping up the voltage of the lasers. Once the optimal power output for each laser was achieved they were shut off and the sample was moved to the desired heating spot; then the

lasers would be turned on again to the same power output to heat the sample. Minor adjustments were made to the power output and optics during heating to adjust for drifting temperatures, to keep the temperature as stable as possible. The lasers were shut off after the desired length of time had elapsed. The heating values were recorded and processed using Black V5 software for the spectrometer, and 4color software for the imaging radiometry (*Black V5*, Oliver T. Lord, University of Bristol, 2017; *4color*, Oliver T. Lord, University of Bristol, 2017).

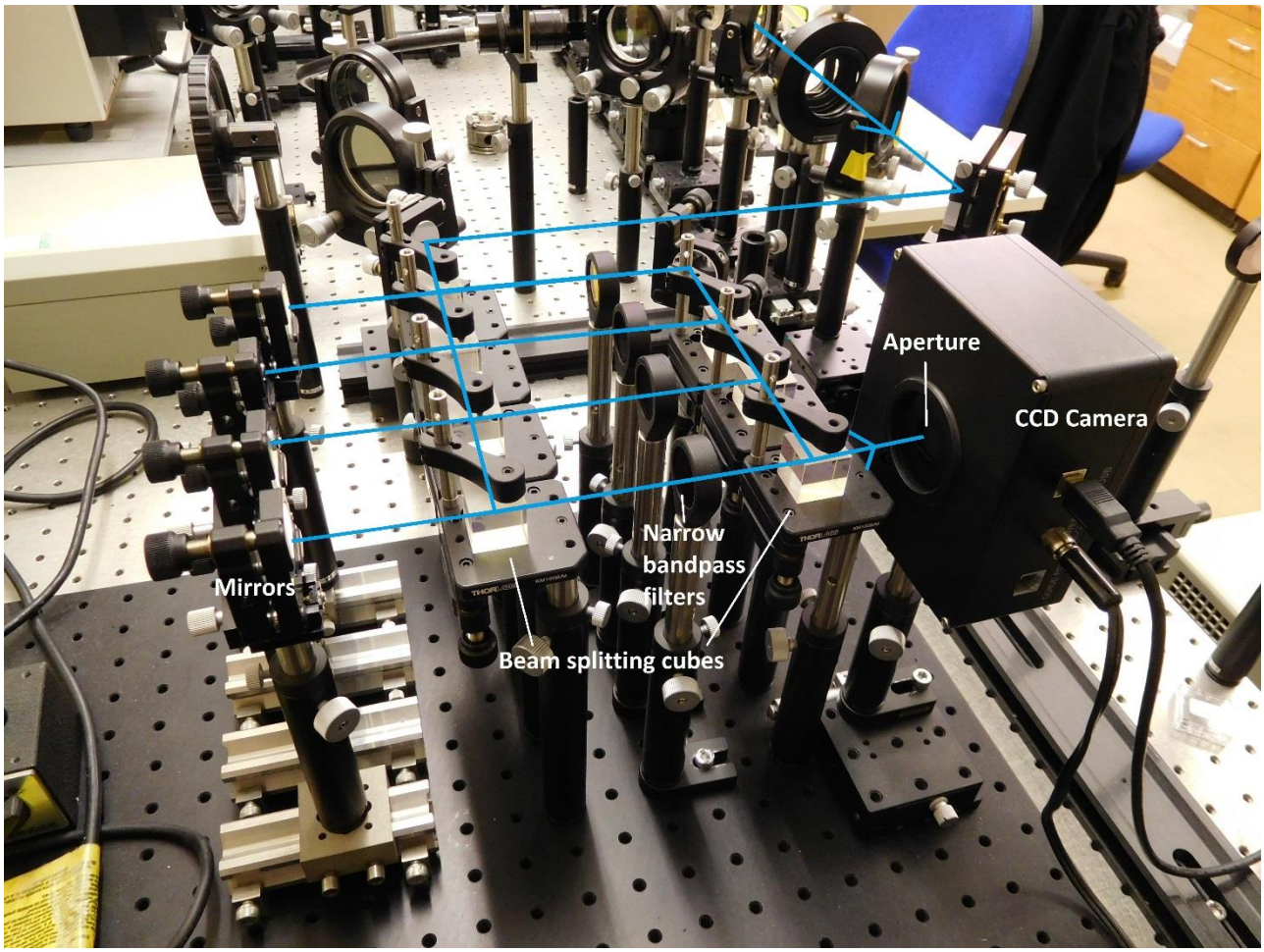

Figure 2.8: the 4color set up used to map temperature, which uses a system of beam splitting cubes, mirrors and narrow bandpass filters to create four images of the sample at different wavelengths, which is captured with a CCD camera (Campbell, 2008). The blue lines indicate the optical pathways.

2.3.3 Final PTt conditions

A total of nine experiments were successfully loaded and heated at the University of Bristol, including three hcp phase experiments; a blank which was pressurise but not heated was also prepared. The details of each experiment are listed in table 2.1, and shown on the phase diagram in figure 2.9.

Table 2.1: the pressure, temperature, phase and time conditions for each sample, note that sample 7 is a blank and was not heated.

Sample	Pressure (±0.2) GPa	Pressure after heating (±0.2) GPa	Temperature (± 40) K	Heating time (s)	Phase
MS_01	40.8	43.6	1900	108	fcc
MS_02	39.5	43.6	2200	110	fcc
MS_03	64.0	71.5	2500	210	fcc
MS_04	77.8	78.5	2200	1200	hcp
MS_05	25.2	27.6	1800	270	fcc
MS_06	72.2	77.7	1900	6935	hcp
MS_07	32.0	32.0	n/a	n/a	bcc
MS_08	52.2	55.0	2200	480	fcc
MS_09	28.5	29.5	1900	190	fcc
MS_10	65.1	63.6	2000	4080	hcp

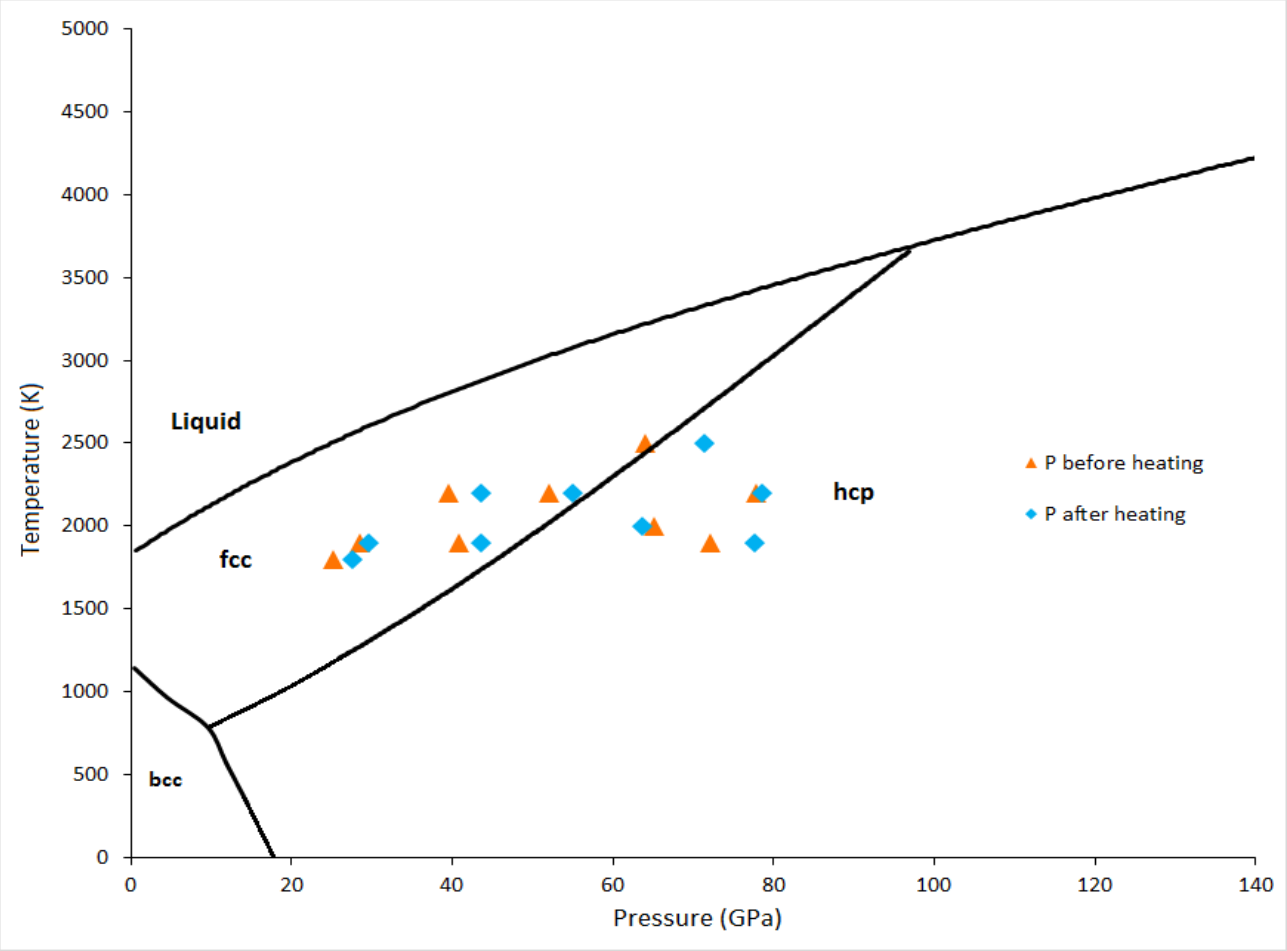

Figure 2.9: a phase diagram showing sample conditions before heating and after. The phase diagram was made using data from Anzellini *et al.*, 2013; and Komabayashi and Fei, 2010, as in situ x-ray diffraction was not used the phase present in each experiment is not certain, the phase boundaries in this diagram were used to determine the phase.

2.4 Analysis

2.4.1 Focused ion beam

The Helios NanoLab G3 CX focused ion beam (FIB, pictured in figure 2.10), located at the Centre for Microscopy, Characterisation and Analysis at the University of Western Australia, was used to extract sections of the samples and prepare them for Nano SIMS. The FIB was used to cut and lift out sections of the iron samples from the locations which had been laser heated, the lift out process is shown in pictures in figure 2.11.

To cut out a section the first step was to deposit a protective layer of platinum onto the sample during which the beam was running at 30 kV and 0.23 nA; the platinum layer had the dimensions: x - 20 µm, y - 2 µm and z- 1 µm. The ion beam was then used to cut two 10 µm deep trenches on either side of the platinum strip, the sides of these trenches were then cleaned so that they were at the edge of the platinum strip.

The stage was then rotated so that the beam could cut along the edge and underside of the section being lifted, leaving one side partially intact to keep it attached to the rest of the sample. The next step was attach a needle so that the section can be lifted out, this was done using a platinum weld from the ion beam. Once the section was welded the final side connecting it to the rest of the sample was cut using the ion beam. The sample is then lifted out and lowered onto a copper v-shaped mount, it is then welded on to with platinum, before the weld connecting the needle is cut. The final stage of sample preparation is to polish the sides of the sample using the ion beam, this was done using a gentle beam, at 5 kV and 86 pA.

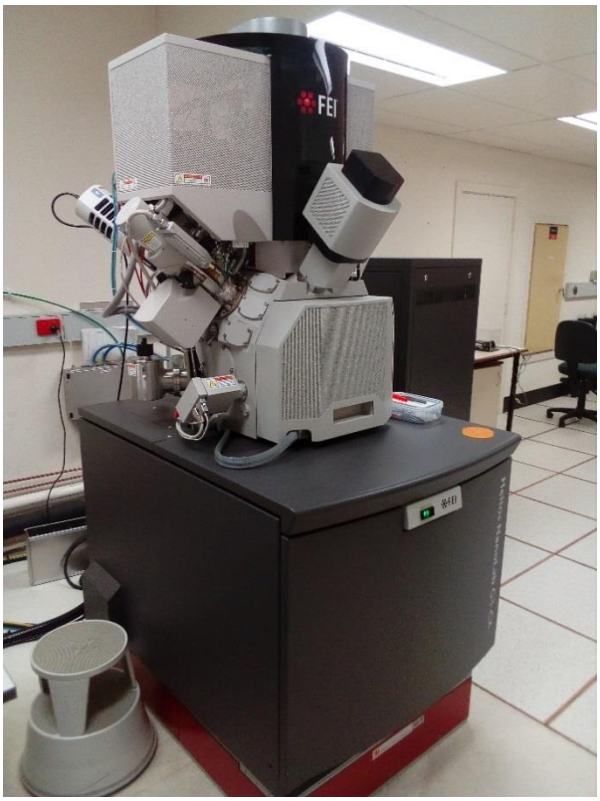

Figure 2.10 shows the FIB located at the Centre for Microscopy, Characterisation and Analysis at the University of Western Australia.

2.4.2 Nano secondary ionisation mass spectrometry (NanoSIMS)

The CAMECA NanoSIMS 50L at the University of Western Australia's Centre for Microscopy, Characterisation and Analysis was used to create elemental and isotopic maps of the sample sections prepared using the FIB. A Hyperion (H200) RF plasma oxygen ion source was used to generate the oxygen$^-$ beam which was used to make the ^{39}K, ^{56}Fe and ^{57}Fe maps. The beam was operating with a current of approximately 14 pA and had a spot size of approximately 100 nm. Prior to each analysis, every area was pre-sputtered with the primary beam to a dose of > 1 x 10^{17} oxygen ions/cm^2. Images were carried out with a raster size of 10-22 um^2, with a resolution of 256 x 256 px and dwell times of 20-80 ms per pixel. Image analysis was carried out using the OpenMIMS Fiji plugin (OpenMIMS, Benson *et al.*, Harvard, 2017).

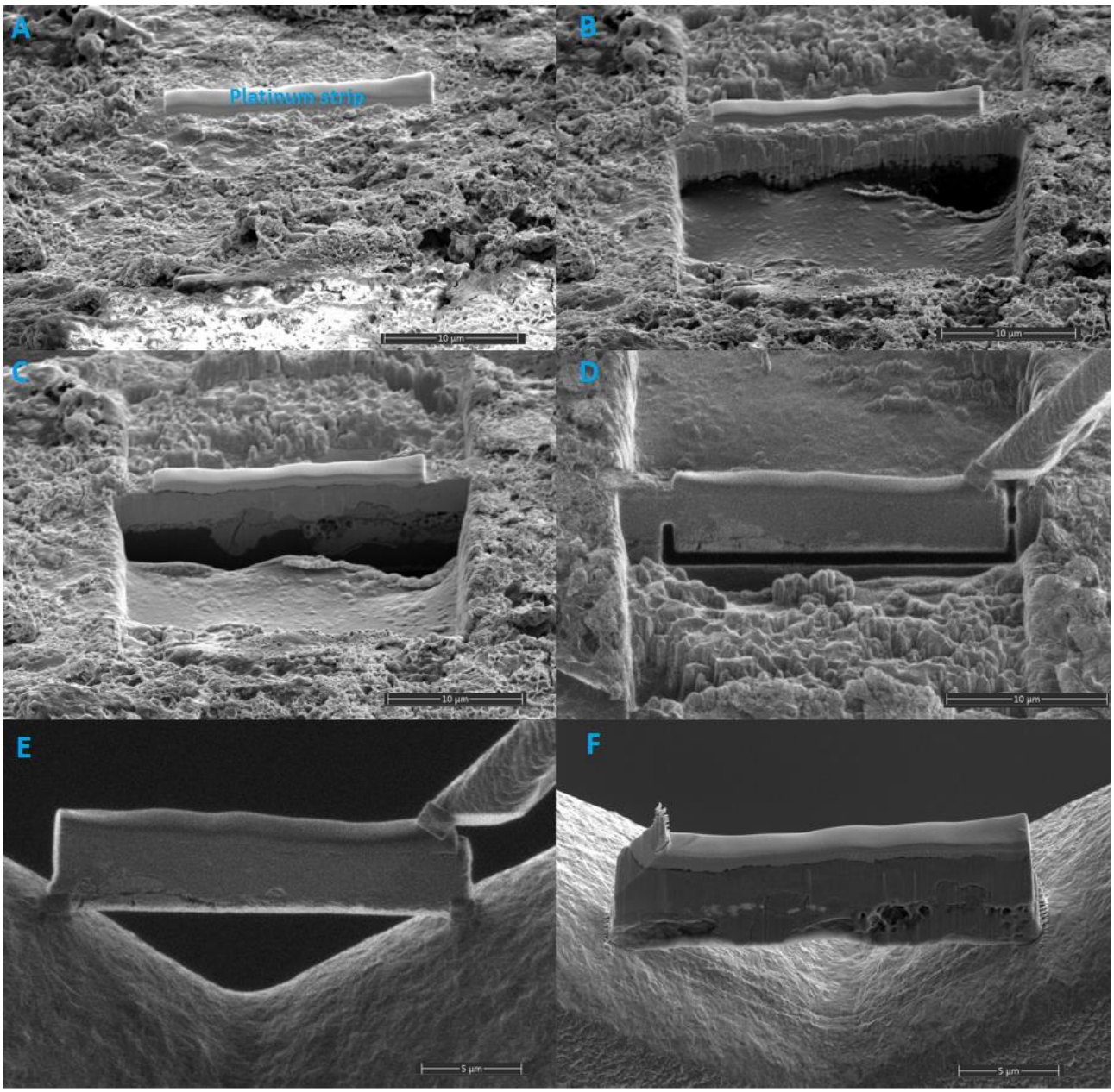

Figure 2.11: a panel of images detailing the sample lift out process in the FIB. Image A shows the platinum strip deposited on the iron surface, B shows the rough-cut trenches before cleaning, and C shows these trenches after cleaning. The needle is visible in image D, where the sample has been undercut and welded to the needle, image E shows the sample being welded to the copper v after being lifted out, and image F shows the final polished section, with the needle weld removed.

3. Results

3.1 Measuring diffusion of samples

Only one sample was recovered from the KCl and successfully lifted out using the FIB; sample MS_02, a fcc phase sample at 43.6 GPa and heated to 2100 K. Processed nanoSIMS images of sample MS_02 are shown in figures 3.1 and 3.2, these images both show a ^{57}Fe enriched curve on one side; this curve is thickest in the centre of the sample and thins towards the edges. The section of the sample where the ^{57}Fe layer is thickest at the centre of the laser heating location, where the

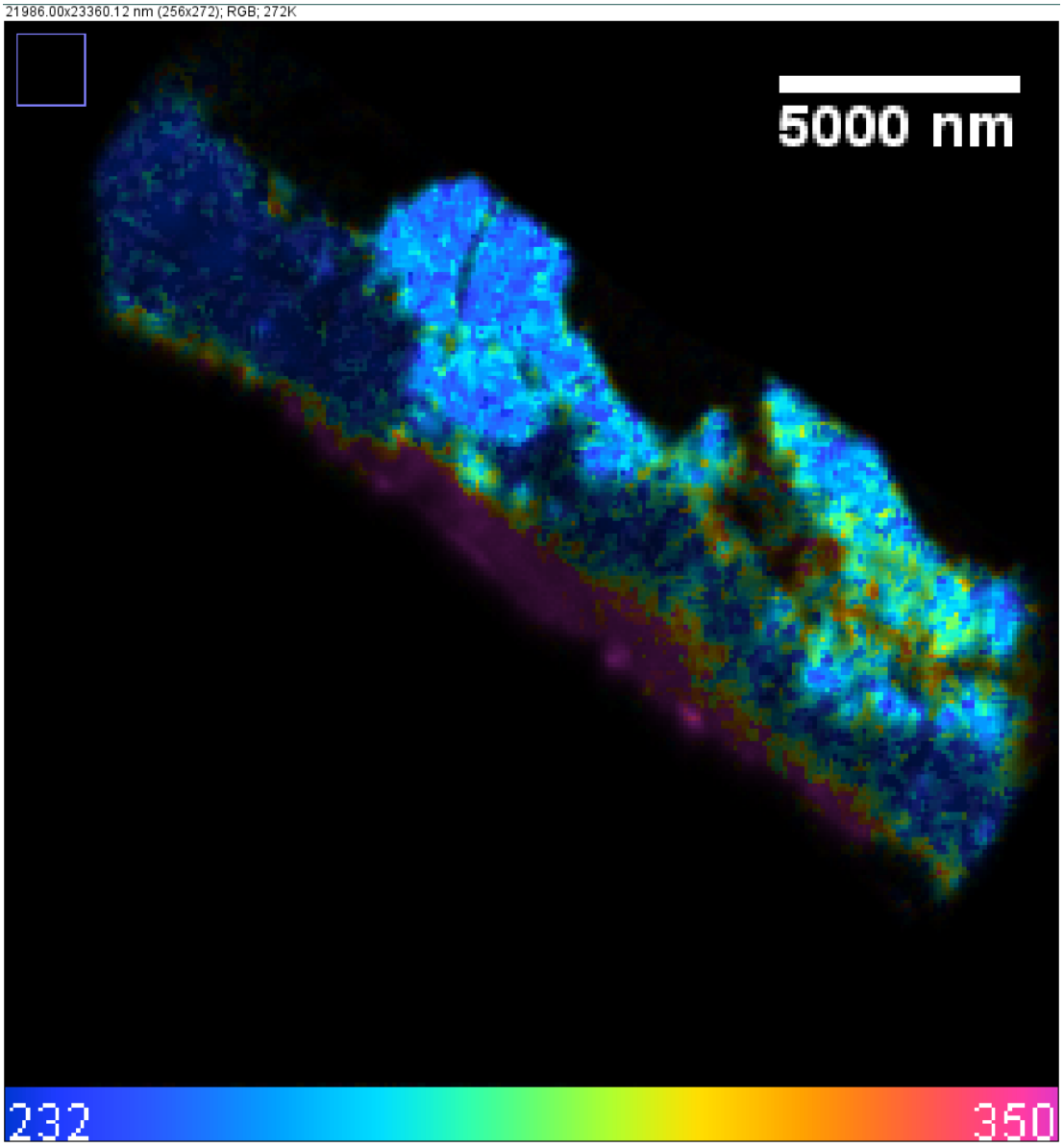

Figure 3.1 is a colourised image showing the ratio of ^{57}Fe and ^{56}Fe for sample MS_02, where pink/red colours indicate higher than normal quantities of ^{57}Fe, and blue colours indicate background levels of ^{57}Fe.

temperature was highest and diffusion was quickest. The ^{57}Fe has diffused about 1.288 µm into the sample, with slight variations depending on where the measurement is taken, $^{57}Fe/^{56}Fe$ ratios for four transects of the sample are shown in figure 3.3. To calculate the diffusion coefficients were determined using the Boltzmann method for each of the transects, this is described in equation 6, where *D* is the diffusion coefficient, *C'* is the integer of the concentration, *t* is the time, *dx* is the distance in microns, and *dC* is the concentration at a given location (Yunker and Van Orman, 2007). From calculating the slopes of the transects in figure 3.3 from the peaks to the background levels (from the flat part of the transects this is where the ratio of $^{57}Fe/^{56}Fe$ is about 270). It was found that at 2100 K and 43.6 GPa the diffusion coefficient was on average 1.46×10^{-14} m^2/s.

(6) $$D(C') = -\frac{1}{2t}\left(\frac{dx}{dC}\right)_{C'} \int_0^{C'} x\,dC$$

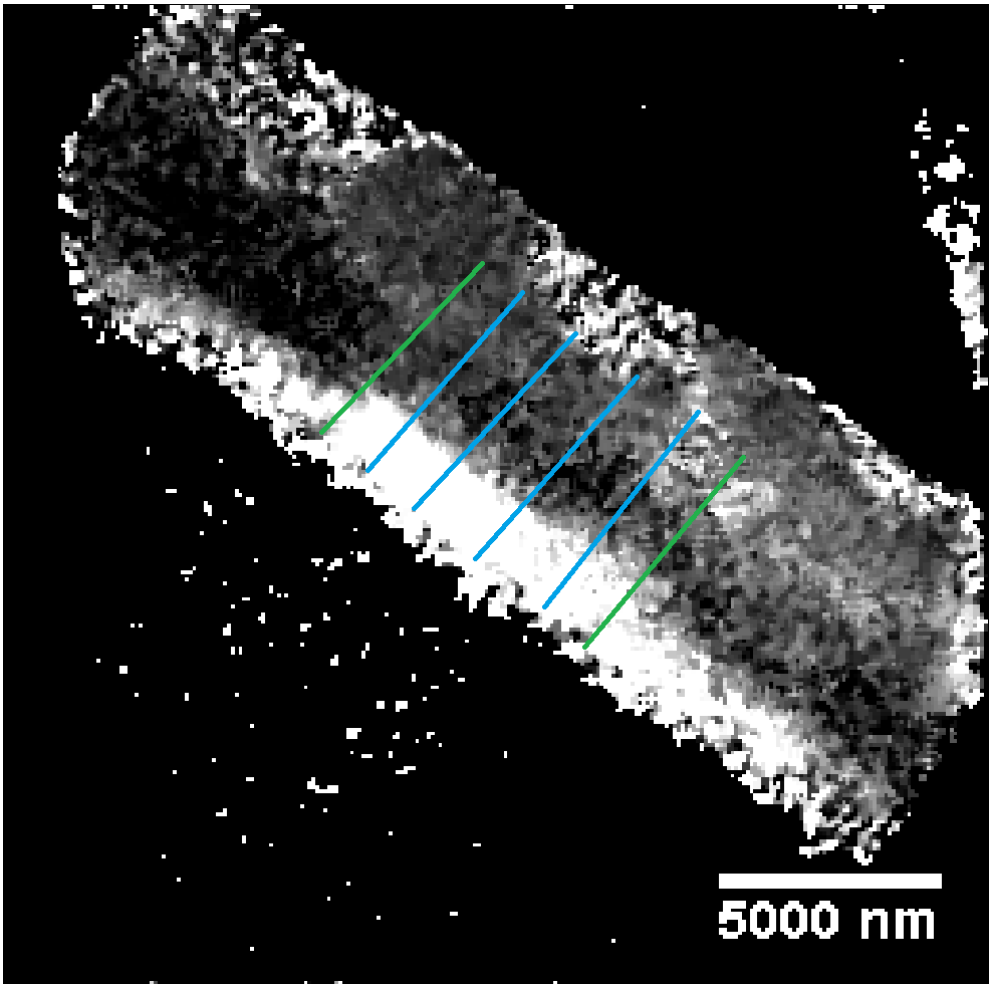

Figure 3.2 is a greyscale image showing the ratio of $^{57}Fe/^{56}Fe$ for sample MS_02, where whiter areas are enriched in ^{57}Fe. Blue lines show the locations of the transects along the main heating spot, while green lines show the locations of transects at the edge of the heating spot.

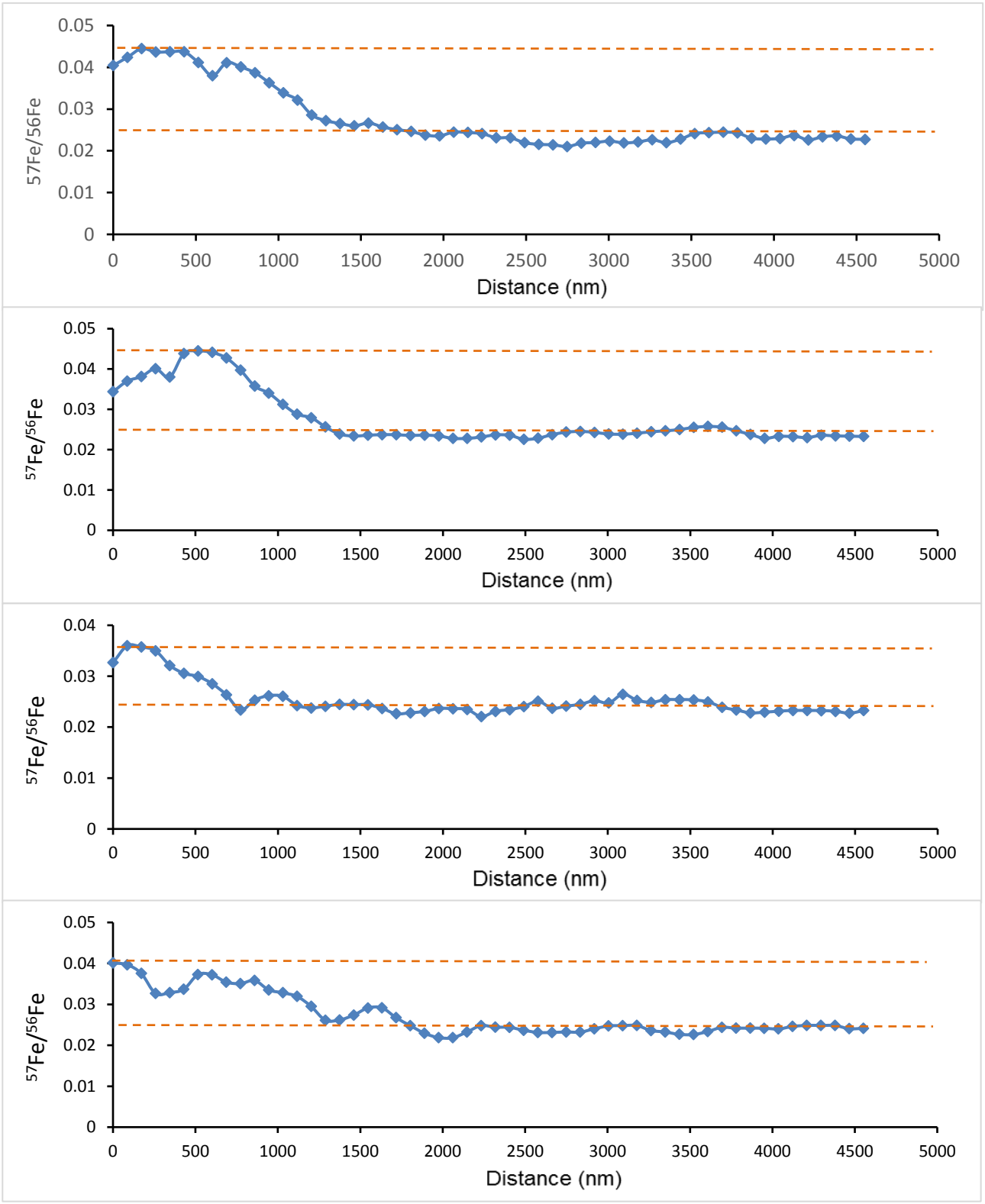

Figure 3.3 shows $^{57}Fe/^{56}Fe$ ratios at varying points along the sample where the temperature was highest. The ^{57}Fe concentration is highest along the left of the profiles, gradually decreasing to background level ratios of about 0.022 $^{57}Fe/^{56}Fe$ at roughly 1500 nm into the transect. Diffusion coefficients were calculated using the slope of the lines between the peak and background levels, indicated with dashed orange lines. On some profiles there is also a decrease in ^{57}Fe to the left of the peak, with a relatively symmetric slope, this might be due to the thicker layer of ^{56}Fe passing through the thin ^{57}Fe layer and pooling on the other side, while the ^{57}Fe continues to shift to the right.

The transects in figure 3.3 have significant variations and bumps, in some cases this appears to be due to one or two inaccurate data points, however some of this may be explained by the potentially uneven nature of the ^{57}Fe coating method or impurities within the sample. This does not appear to affect the gradient of the slope from the peak ^{57}Fe to background ^{57}Fe values along the transects, which in all cases fairly linear and did not vary too much between transects.

A second diffusion measurement at lower temperatures was also made using the sample MS_02. This required using the temperature maps from the 4color system to estimate the temperatures at a certain distance from the centre of the heating spot; in this case the temperature was measured at 3.5 microns from the centre, using heat maps such the one featured in figure 3.4, the temperature was averaged for 15 of these temperature maps. Error maps were also used to estimate the averaged error of the temperature maps, figure 3.4 also shows one of these error maps. The temperature at 3.5 µm from the centre of the heating spot was found to be 2000 K, with an error of ±24 K. transects of the diffusion profile were made 3.5 µm on either side of the central heating spot, these transects are shown in figure 3.5; the diffusion coefficient at these locations was calculated to be 9.92×10^{-15} m^2/s.

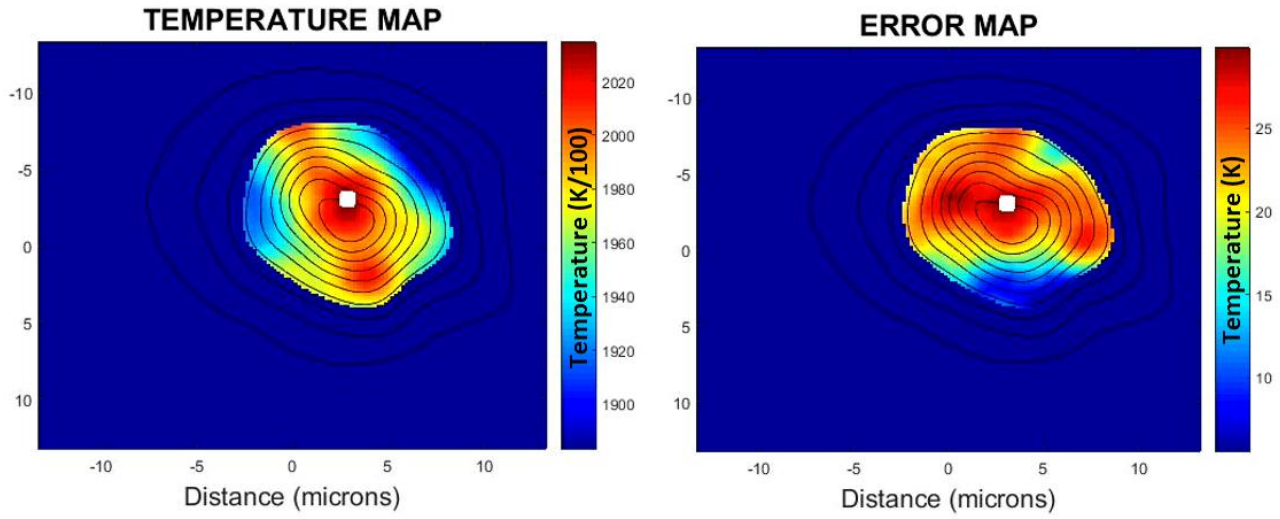

Figure 3.4 shows example temperature and error maps recorded during the heating of sample MS_02, a total of 15 sets of these images were used to estimate the temperature at 3.5 µm from the central heating point.

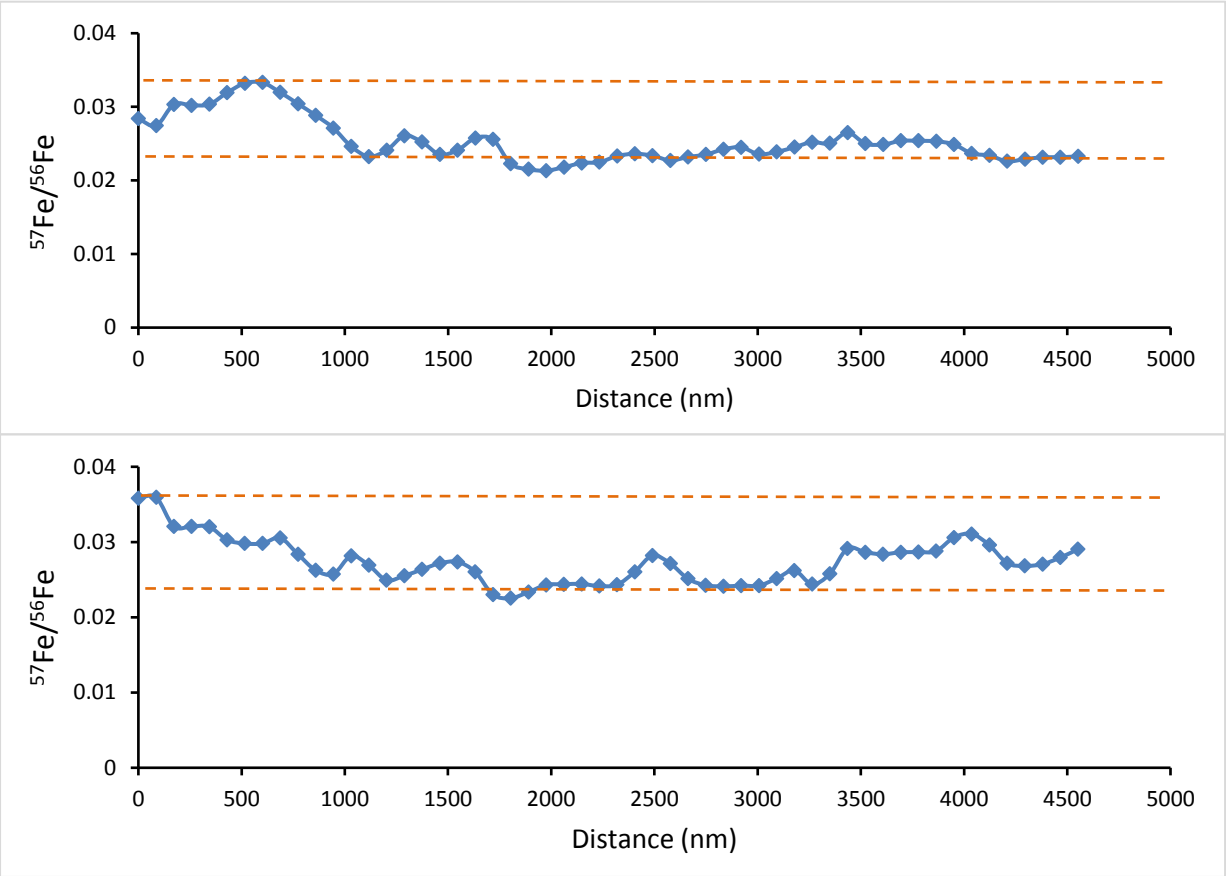

Figure 3.5 shows the $^{57}Fe/^{56}Fe$ ratios at either side of the heating spot, at a distance of 3.5 microns from the centre, the temperature at this distance from the centre of the laser was approximately 2000 K. The diffusion rate at this distance and temperature was used to generate a second diffusion measurement from the same sample.

3.2 Plotting diffusion measurements with existing data

Once diffusion values had been determined it was then necessary to plot the diffusion coefficients from this study against that of previous studies, to see if the values are reasonable and if there are any obvious trends in the data. The effect of temperature on the diffusion coefficient can be seen in figure 3.6, and the effect of pressure can be seen on figure 3.7.

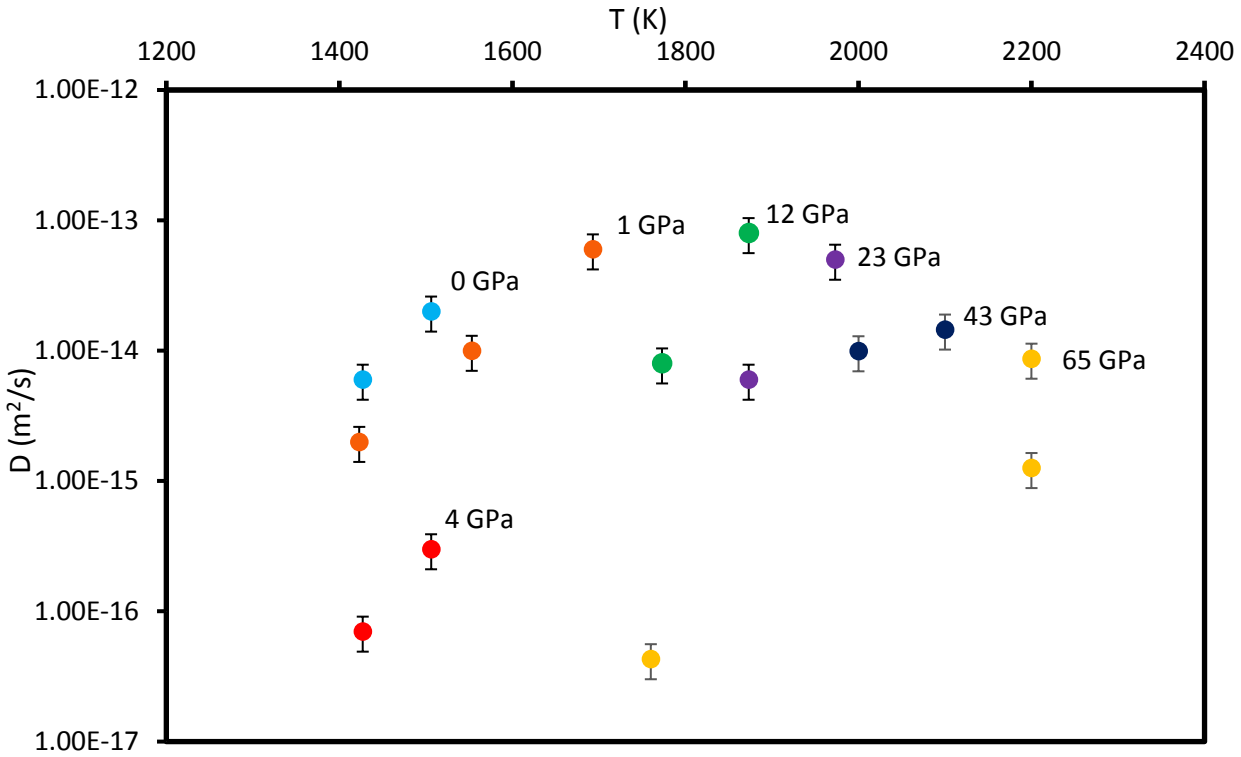

Figure 3.6 is a plot of diffusion coefficient versus temperature, with variations in pressure labelled (Goldstein *et al.*, 1965; Yunker and Van Orman, 2007; Reaman *et al.,* 2012).

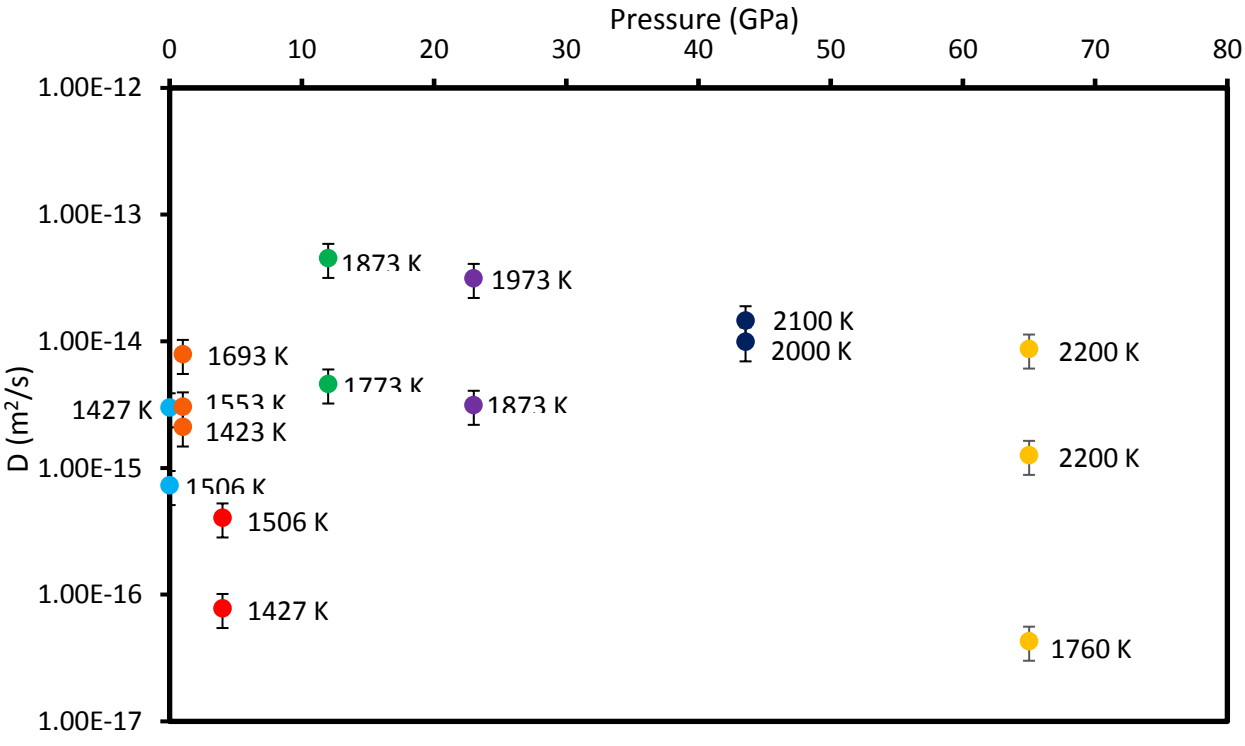

Figure 3.7 is a plot of diffusion coefficient versus pressure, the temperature for each measurement has also been labelled (Goldstein *et al.,* 1965; Yunker and Van Orman, 2007; Reaman *et al.,* 2012).

4. Discussion

4.1 Comparison with existing data and models

In this study the diffusivity of iron was measured at 43.6 GPa, nearly double the pressure of the previous diffusion experiments which use a multi-anvil, and the only experiment to measure diffusion of pure iron in a DAC (Reaman et al., 2012; Yunker and Van Orman, 2007). Given the much higher pressures at which the experiment was conducted, it is not surprising that the measured diffusion coefficients do not perfectly fit the trends expected from the extrapolation of lower pressure experiments.

The main difference between the diffusivity of the sample in this study and the expected result is that the diffusion coefficient is more than two orders of magnitude faster than expected. This difference appears to be a function of pressure, as the temperature of the samples in this study were only a little more than 100 K higher than previous diffusion experiments. Another trend that appears is the apparent decreased effect of temperature with increasing pressure. This is a trend that appears to be affecting the Yunker and Van Orman 2007 experiments at 12 and 23 GPa; with the same temperature difference between the samples of 100 K the two diffusion values at 23 GPa are closer together than those at 12 GPa. This effect appears to be much greater in the sample from this study, with the two diffusion values being close (9.92×10^{-15} m^2/s at 2000 K vs 1.46×10^{-14} m^2/s at 2100 K) despite the 100 K temperature difference.

The data was then plotted for diffusion versus pressure, with temperature isotherms generated using calculations from Yunker and Van Orman, 2007 (figure 4.1), Sammis and Smith, 1981 (figure 4.2), and Zhang, 2014 (figure 4.3). The values predicted by Sammis and Smith's 1981 calculation are consitently slower than the values measures at pressures greater than a few gigapascals, however they are moderately successful at predicting lower pressure values. The Yunker and Van Orman, 2007 model shows some improvement at predicting diffusion values at higher pressures, although some measurements are still nearly an order of magnitude faster than the model predicts; the accuracy of predicting the low pressure values shows little or no improvement upon the Sammis and Smith, 1981 model. The cΩB model from Zhang, 2014 is by far the most reliable at predicting the higher pressure diffusion rates, however it is unable to predict the diffusion rate of iron in either the hcp phase or the bcc phase, so the existing lower pressure measurements should not be compared with this model.

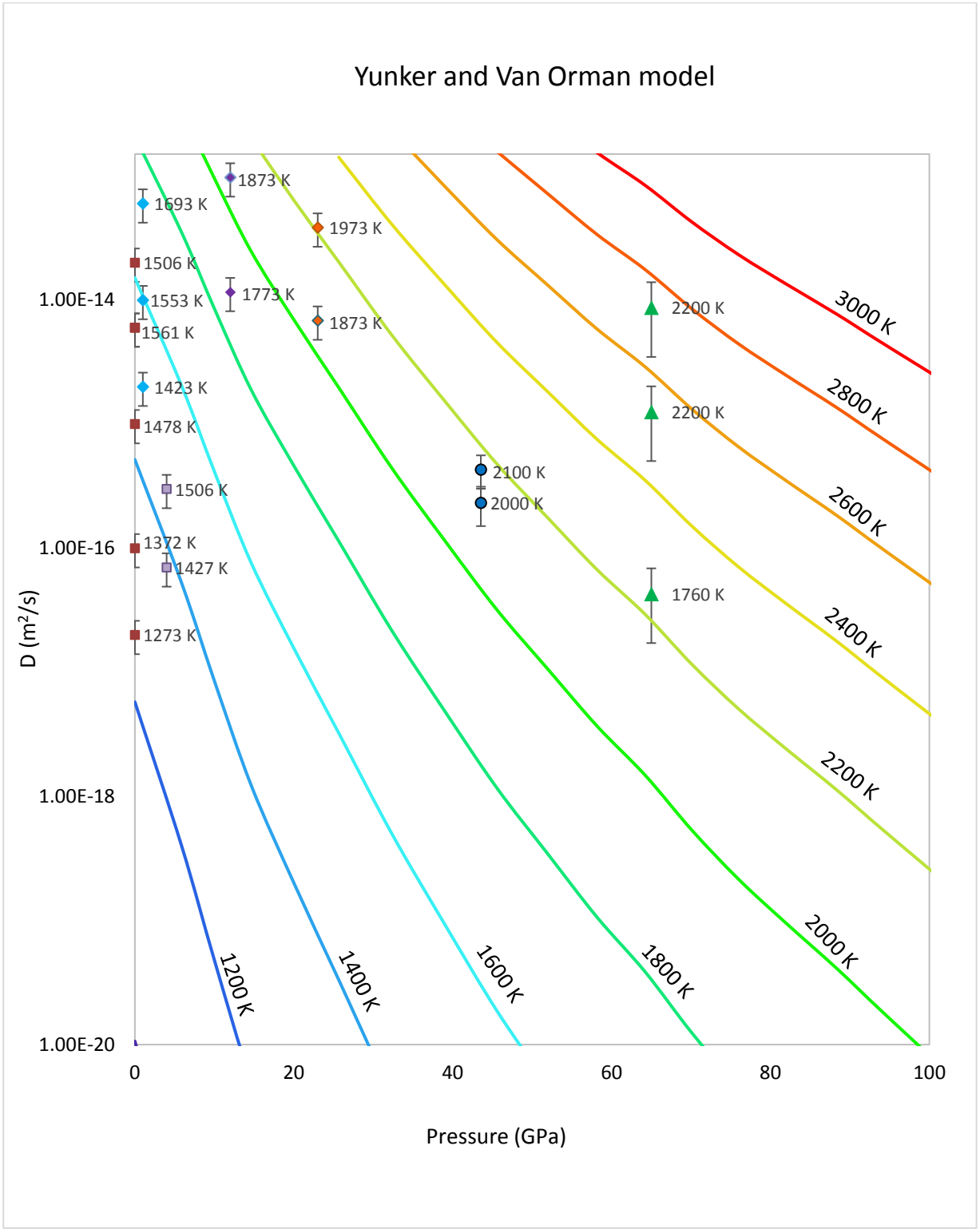

Figure 4.1 shows the diffusion coefficients from this study, Goldstein et al., 1965, Yunker and Van Orman, 2007, and Reaman *et al.,* 2012. The isotherms showing what the diffusion should be at a given temperature have been calculated using equation 3, with the melting point of iron at different pressures being taken from figure 3 of Anzellini et al., 2013 in order to run the calculations. Measurements with square markers come from Goldstien *et al.*, 1965, diamonds come from Yunker and Van Orman, 2007, triangles indicate Reaman *et al.,* 2012 and circles indicate measurements form this study.

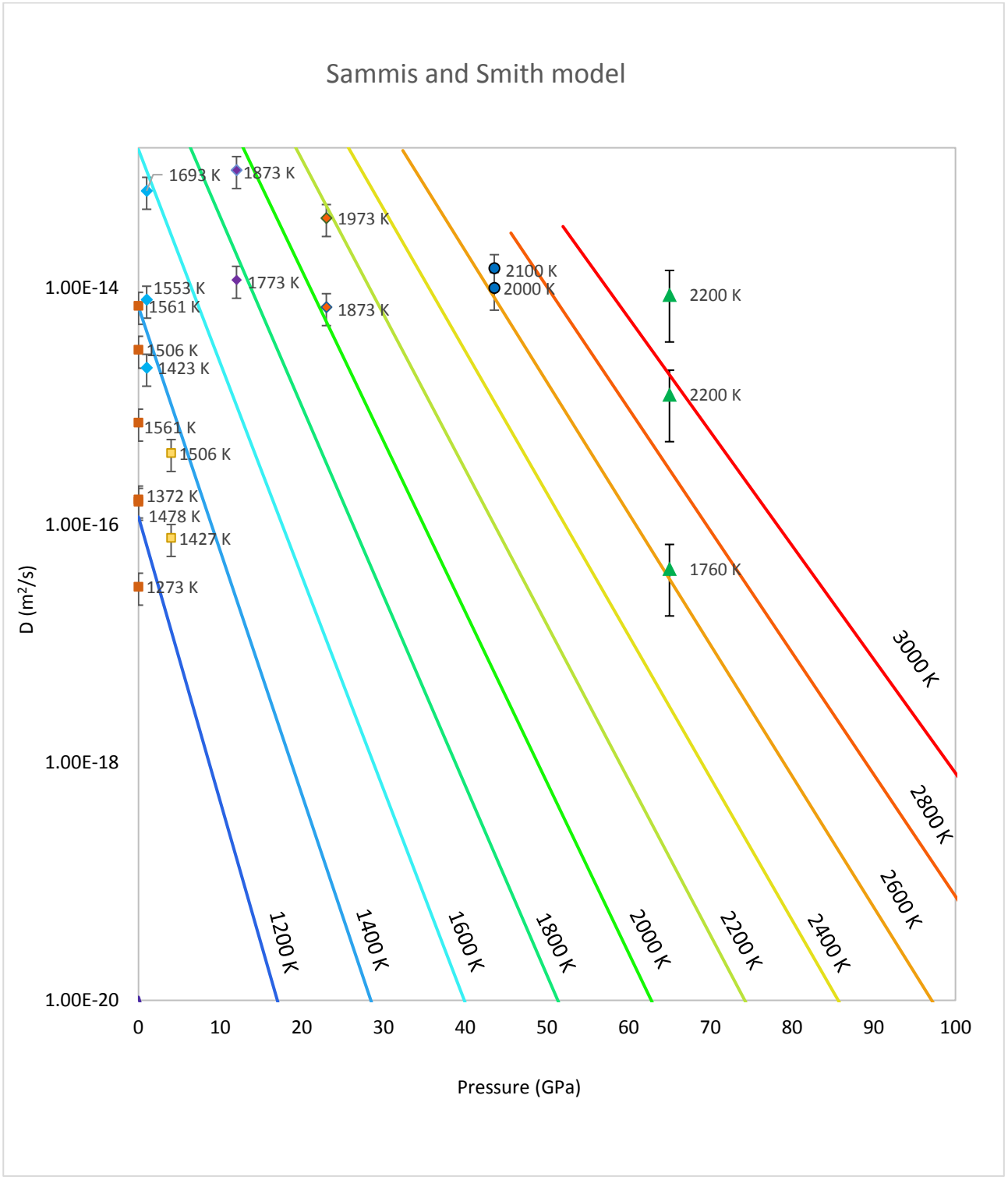

Figure 4.2 shows the measured diffusion coefficients, this time plotted with isotherms calculated using equation 1 (Sammis and Smith, 1981).

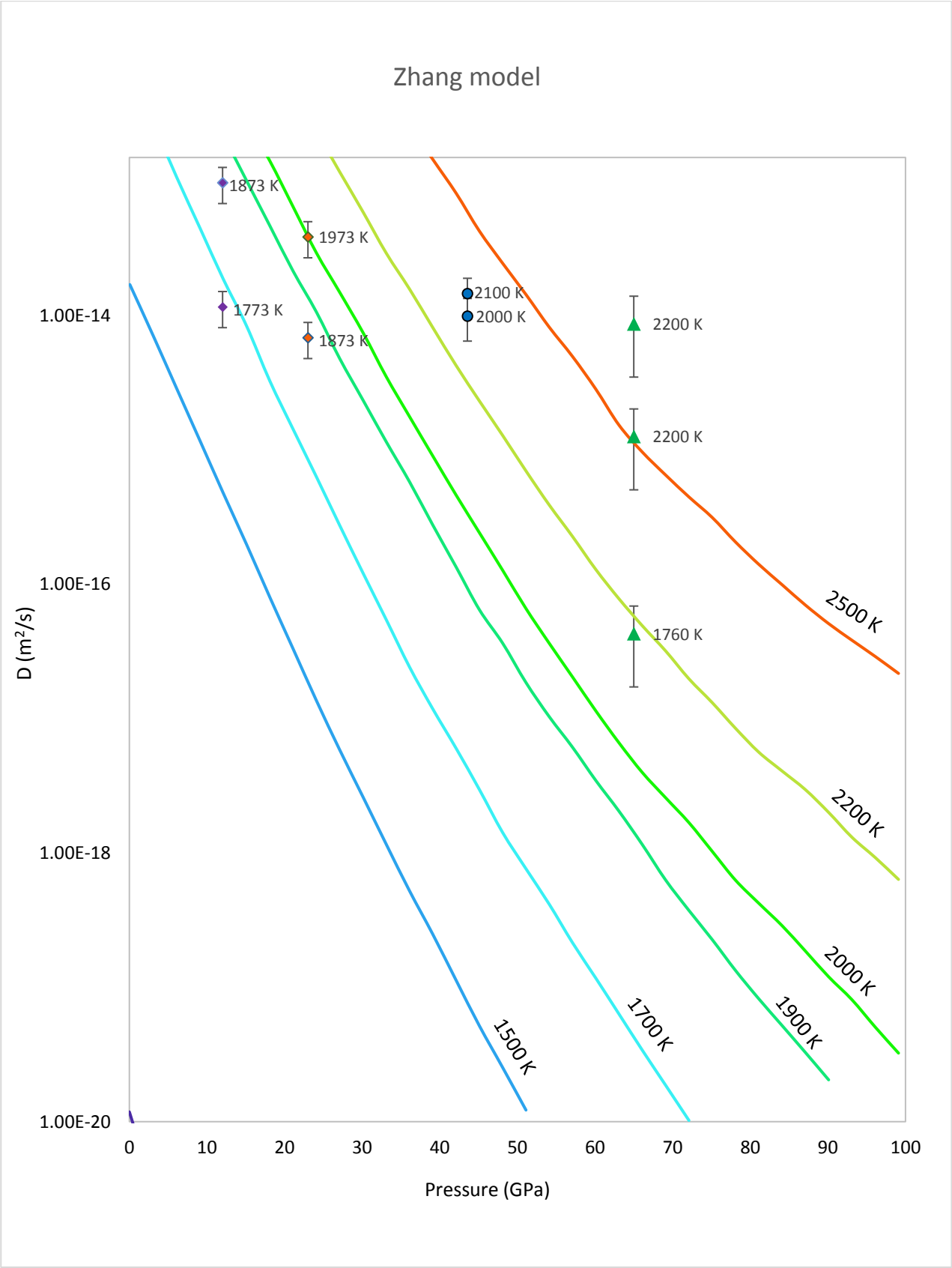

Figure 4.3 displays the calculated diffusion coefficient isotherms taken directly from Zhang, 2014, these isotherms were taken from the hcp (ε iron) plot, which is actually a plot generated from a fcc iron measurement.

4.2 Assessing the accuracy of theoretical models

Of the three diffusion models discussed in this study in section 1.4, and shown in figures 4.1, 4.2 and 4.3 the best fitting appears to be the Zhang, 2014 model. Although the cBΩ model is the least inaccurate of the three pre-existing models discussed in this study, it is also the most limited in scope, as it can only be applied to the fcc phase using Zhang's 2014 calculations. The cBΩ model in figure 4.3 was still not able to accurately predict all of the fcc samples, with the higher-pressure sample from this study, and those from Reaman *et al.,* 2012, having a much higher diffusion coefficient than predicted. Given that it only has a moderate level of accuracy it is not ideal to keep using the same model, as it uses iron-nickel diffusion to generate the values (Zhang, 2014). It may be that the cBΩ model could be revised to include the new iron self-diffusion values from this study and see if the model is robust.

The model derived from the Sammis and Smith's 1981 paper (see equation 1, figure 4.2) is perhaps the least satisfactory of the three. This may be because it does not take into account that the change in diffusion rate with pressure is not constant. Therefore, the model works at the low-pressure conditions explored at the time the paper was published, but does not fit the higher-pressure data from later studies, and consistently underestimates these values.

The model from the Yunker and Van Orman, 2007 (see equation 3, figure 4.1) is more reliable at predicting the diffusion rate at a greater range of pressure and temperature conditions. It does this because the pressure component of the equation is incorporated as a part of the melting temperature component of the equation. As the pressure increases the melting temperature increases, so the model predicts higher diffusion rates at higher pressures, where the Sammis and Smith, 1981 equation fails. Despite this the model is still flawed, it still makes low predictions of diffusion values at higher pressures, and does not offer any advantage at predicting diffusion values at lower pressures. In part, this may be attributed to an assumption that at a constant ratio of T/T_m there would be no effect of increasing pressure, and therefore no further adjustment of pressure in the equation 3 was needed (Yunker and Van Orman, 2007). With the diffusion measurements made in this study this was found not to be the case, with the values at 43 GPa having slightly higher diffusion rates than was predicted when adjusted to the same T/T_m ratio, this is shown in figure 4.4. Due to the effect of pressure not being constant it would be necessary to add another pressure component to equation 3 to make it accurate at predicting diffusion at high pressures.

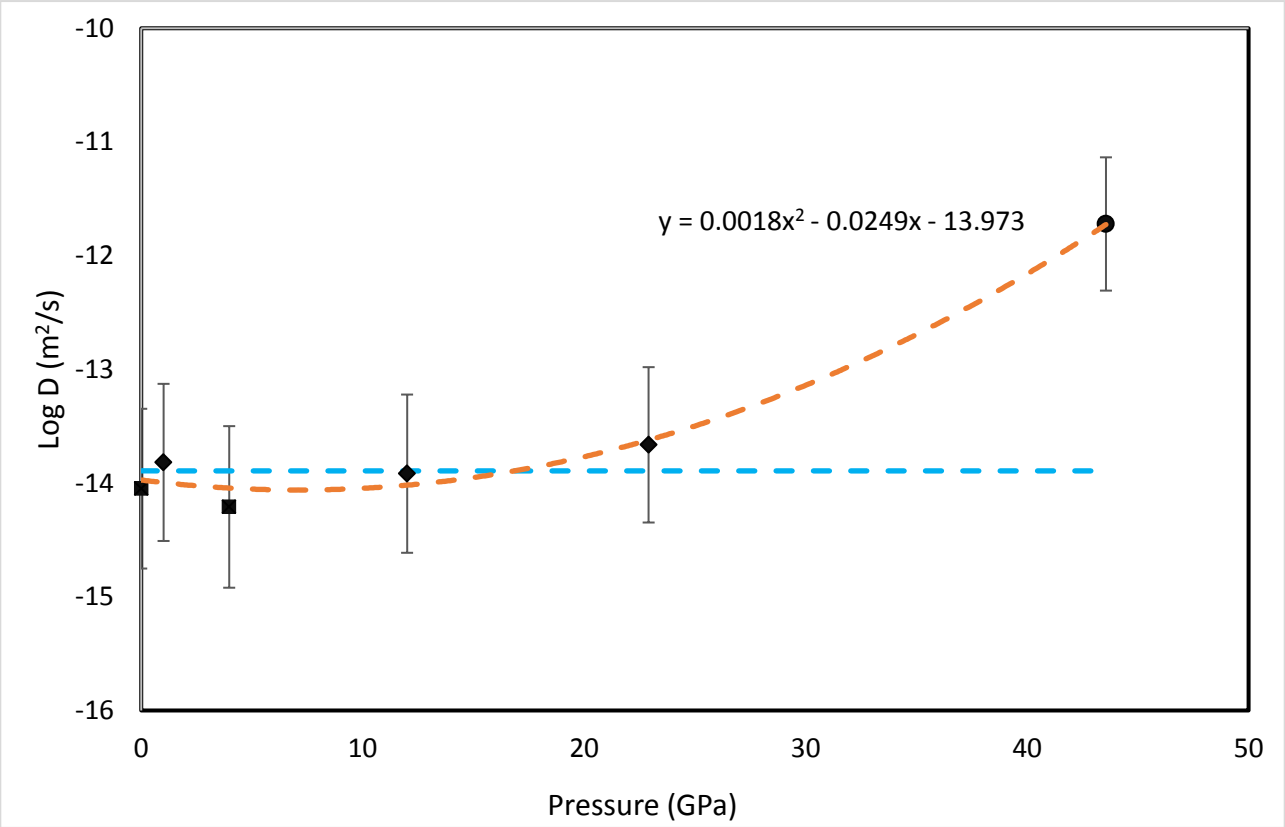

Figure 4.4 is adapted from figure 9 from Yunker and Van Orman, 2007; the log diffusion coefficients from their own nickel iron experiments (indicated with diamonds), as well as two from Goldstein *et al.*, 1965 (squares), and an iron self-diffusion value from this study (circle). All of the diffusion values in this experiment have been normalised so that $T/T_m = 0.874$, the orange dashed line is a trendline including the data from this study, the dashed blue line is the trend line that Yunker and Van Orman, 2007. It would also be possible to fit a straight trendline through this data, however the curve is more accurate. With the added data point from this study it is apparent that the diffusion rate has more variation in pressure than is taken into account by T_m.

Both the Sammis and Smith, 1981 model and the Yunker and Van Orman, 2007 model share a drawback; they do not take into account the different phases of iron. This flaw is not shared by the cBΩ model from Zhang, 2014, which calculates each phase of iron separately, however this does mean that the cBΩ model is only appropriate for estimating diffusion values across a single phase. Due to this limitation, a new calculation needs to be made for each phase; this requires a measured diffusion value from an experiment, which means that the cBΩ model cannot currently be used for predicting hcp iron until there is a successful hcp iron diffusion experiment (Zhang, 2014).

4.3 Revisiting the Sammis and Smith model

The main issue with Yunker and Van Orman's 2007 model is that it does not account for pressure adequately, this is clearly shown in figure 4.4, where adding another data point at much higher pressure has uncovered a trend influenced by pressure. To avoid the inaccuracy at higher pressures experienced by using T_m as the pressure changing function in the equation, it will be necessary to go back to the original Sammis and Smith, 1981 model (equation 1) which was previously modified to add T_m instead of the function pV^*. To calculate the activation volume V^*, figure 4.5 was used, which is a plot of the samples adjusted to a constant temperature of 1600 K, the gradient of the trendline was put into equation 7, giving a V^* of 1.43 cm^3/mol.

(7) $$V = (R * 1600) * 0.1085$$

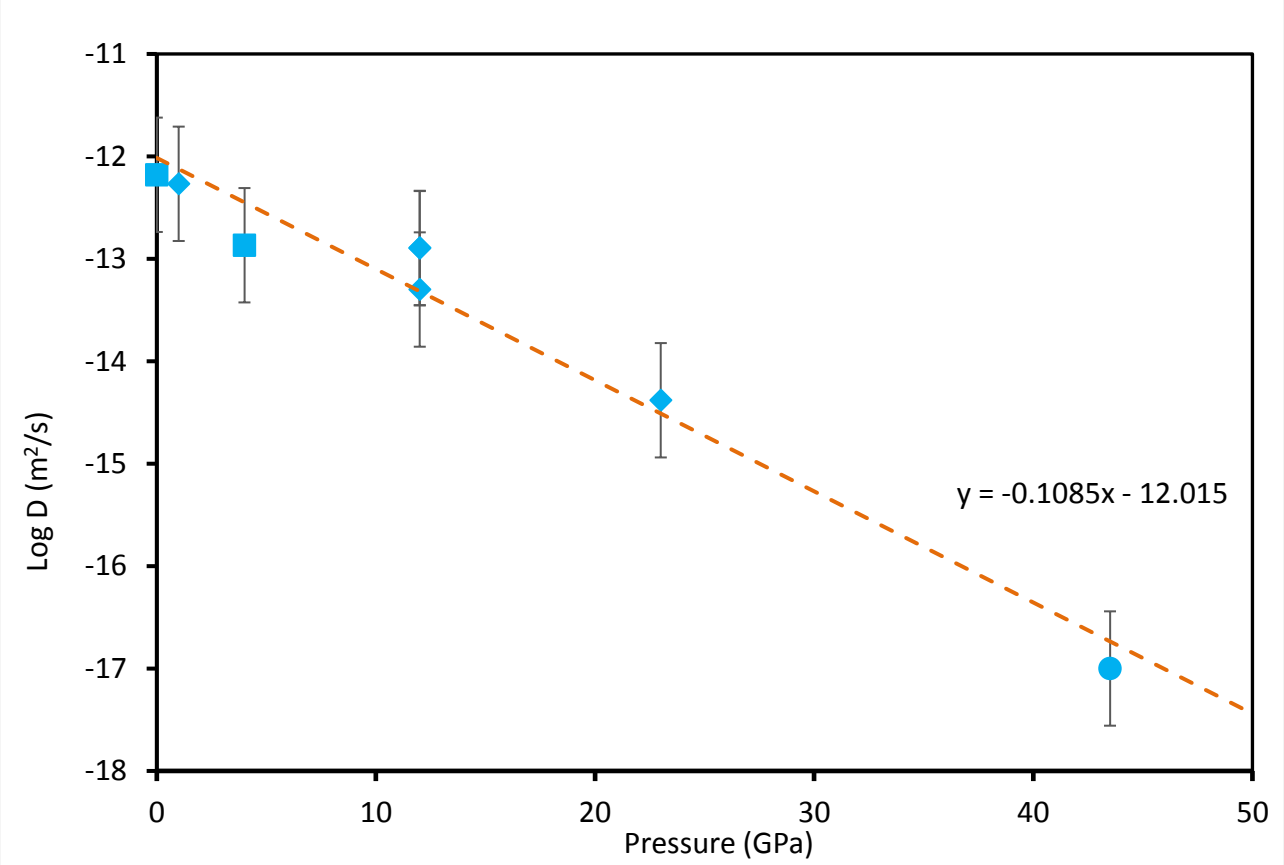

Figure 4. 5 is a plot of the log diffusivity plotted against pressure, with each sample being normalised to a temperature of 1600 K, adapted from Yunker and Van Orman, 2007. Squares represent samples from Goldstein *et al.*, 1965, diamonds show samples from Yunker and Van Orman's 2007 samples, and the circle shows the sample from this study.

The activation volume in this study, 1.43 cm^3/mol, is much smaller than the 6 cm^3/mol in Goldstein *et al.*, 1965, or the 3.1 cm^3/mol in Yunker and Van Orman, 2007. The activation energy *E** was calculated to be 341 kJ/mol, which is higher than the Goldstein *et al.*, 1965 value of 318 kJ/mol or Yunker and Van Orman's 2007 value of 300 kJ/mol. The values calculated from this study were used to recalculate equation 1 at varying temperatures and pressures, in order to plot an updated Sammis and Smith model, shown in figure 4.6.

The updated model in figure 4.6 is much more accurate at modelling the diffusion coefficients of iron at higher pressures than any of the models previously discussed. Most of the diffusion coefficients measured at 12, 23 and 43.6 GPa are within error of the calculated isotherms, so that at high pressures this recalculated model fits the data reasonably well. At lower pressures there are still some values which do not fit well, however this is no better or worse than the previous models, and is likely more of a reflection of the data rather than the model's inaccuracy. A direct comparison between the Sammis and Smith model and the Yunker and Van Orman model is made in figure 4.7, which includes isotherms from both models overlayed on the same plot.

Now that there is a model which can predict, with reasonable accuracy, the diffusion coefficient of iron under mantle conditions it is possible to start making predictions about the behaviour of iron in the mantle and core.

4.4 Implications for the properties of the Earth's mantle and planetary cores

The results of this study have several implications for the behaviour of iron under mantle conditions. The most important finding is that the diffusion of fcc iron is much faster under mantle conditions than previously predicted. This means that at the PT conditions under which planetary cores begin to form (around 20 GPa and 2550 K, conditions under which iron is liquid) solid iron will diffuse much faster, allowing for faster core formation (Kaminski and Javoy, 2013). Faster diffusion of solid iron under mantle conditions also leaves more credibility to the idea that the Earth's core could have formed relatively quickly, even with only a partial magma ocean or the absence of a magma ocean.

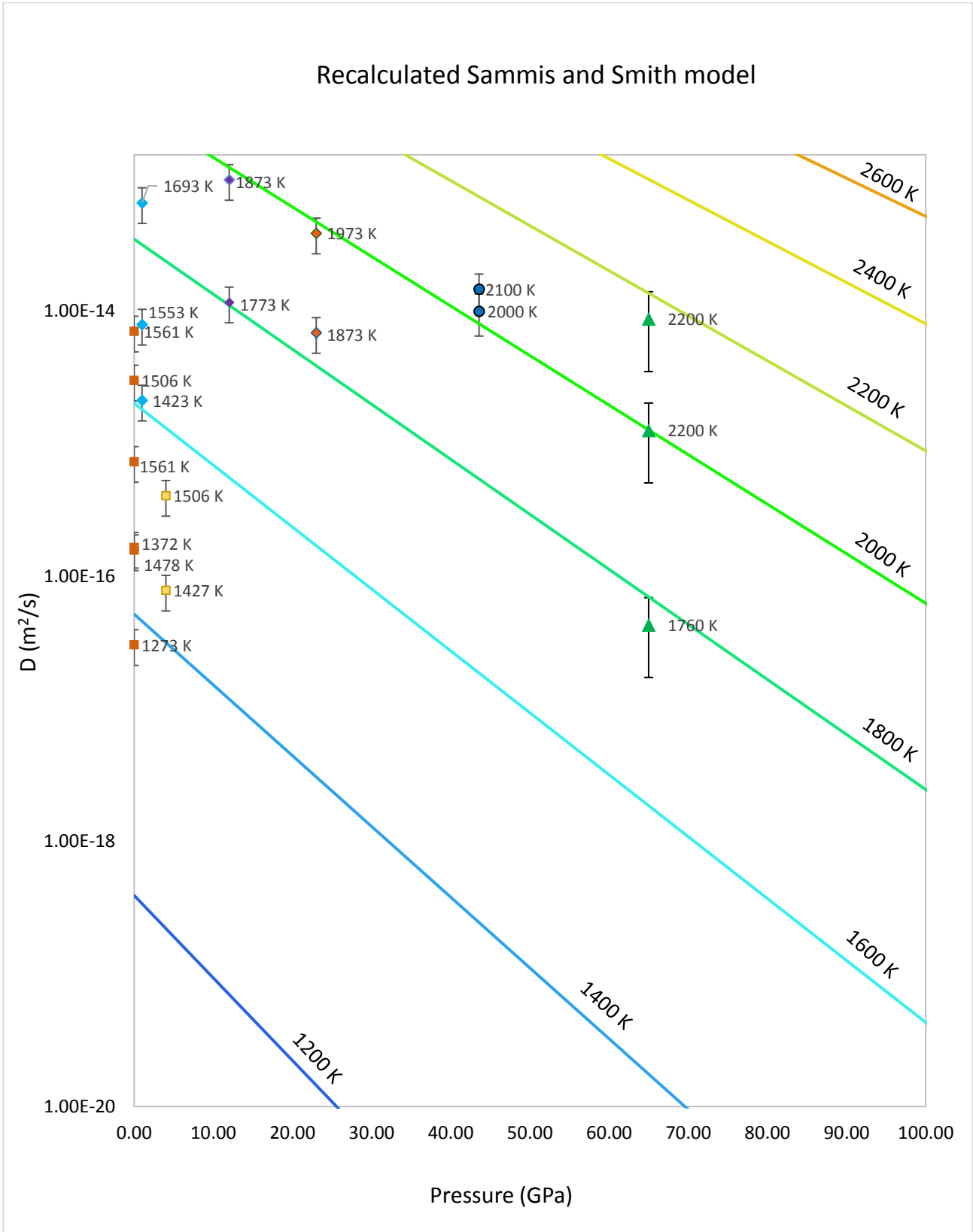

Figure 4.6 uses isotherms recalculated using Sammis and Smith's 1981 model (see equation 1), but using *V** and *E** values from this study, and the D_0 value from Yunker and Van Orman, 2007. All of the diffusion coefficient values at 1 GPa appear to be an order of magnitude or more too fast.

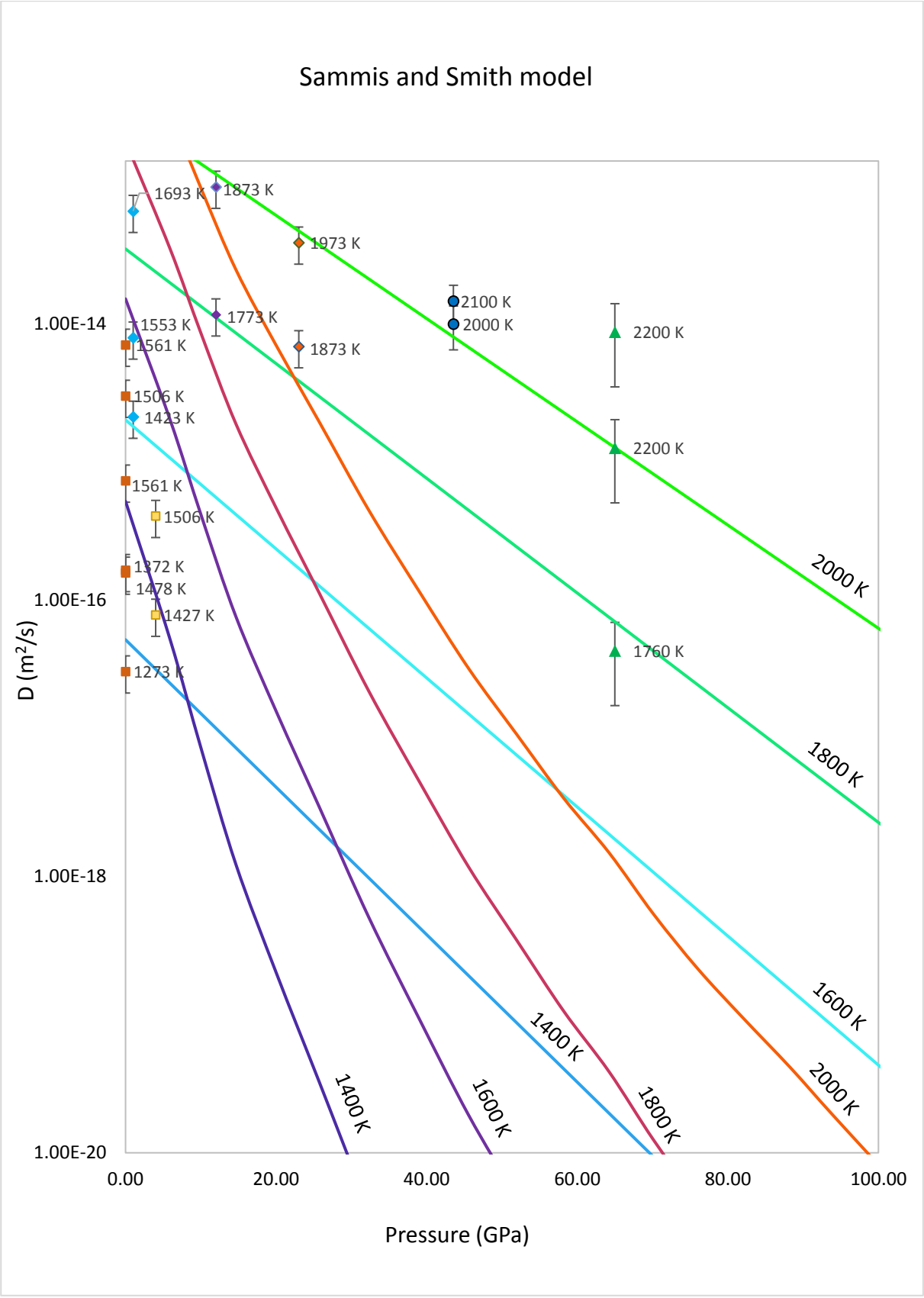

Figure 4.7 is a direct comparison between the models produced using equations from Yunker and Van Orman, 2007 (purple to orange isotherms) and Sammis and Smith, 1981 (blue to green isotherms). Note the greatly improved accuracy at high pressure for the Sammis and Smith, 1981 model.

While it may not be reasonable to extrapolate the diffusion coefficients of this study by 300 GPa and several thousand degrees kelvin to look at the conditions of the Earth's inner core, it is entirely reasonable to use the measurements to look at other planetary cores (Anzellini et al., 2013). The pressure and temperature conditions at the core of smaller planets are much less extreme than those of Earth's core, for example the core of Mars has pressures of around 40 GPa and temperatures of 2200 K, which is directly comparable to the diffusion coefficient measured in this thesis (Kavner et al., 2001; Stewart et al., 2007). At 40 GPa and 2200 K the calculated diffusion coefficient for iron, using equation 1, would be 9.5×10^{-14} m^2/s; this provides a good basis for determining the actual diffusion coefficient for the core of Mars, which has an iron-nickel composition, with a significant sulphur component (Kavner et al., 2001; Stewart et al., 2007). Importantly, at these PT conditions, iron is in an fcc structure, so the results are directly applicable in this case and a hcp measurement is not needed.

Mercury is another planet with PT conditions at its core comparable to the conditions of the sample from this study. The inner core of Mercury has pressures of 30-40 GPa and temperatures <2000 K, so that the self-diffusion coefficient of iron would be around 1×10^{-14} m^2/s (Malavergne et al., 2010). Interestingly, Mercury has a reducing environment, a possibly stratified liquid outer core which generates a magnetic field, and the possibility of iron snowing down towards the solid inner core, Mercury's relatively active interior makes it an interesting case study with possible applications to Earth's core formation (Dumberry and Rivoldini, 2015; Malavergne et al., 2010). Mercury's core is mostly iron, although it also has silicon and sulphur components which reduce the melting temperature of the core so that parts of the core are liquid (Malavergne et al., 2010).

This thesis has shown that it is possible to simulate diffusion in solids at the pressures and temperatures of the Earth's mantle, and the cores of smaller planets. This provides a basis for future studies to determine the extent to which diffusion acts as a rate limiting factor in the geodynamics of planetary interiors.

4.5 Critical reflection

4.5.1 Experiment issues

There were some issues with the experiment design which lead to problems during analysis, most of these are related to the KCl that was used as a thermal insulator and pressure medium. The main issue is that while using the FIB it is not possible to see through the salt layer and see the outline of the sample, making it impossible to locate the heating spot and cut out the right section of the sample.

There were several different methods used to remove the salt from the samples, including dissolving it in deionised water, filtering it and putting the samples in a hypersonic bath. Dissolving the salt was unsuccessful, even after leaving it in water for two days the salt remained unchanged; heating the water was also attempted. Passing water over the sample in a filter also proved passive a way to remove the salt. Putting the gasket with the sample in a hypersonic bath did prove partially successful, as in every case the sample was dislodged from both the gasket and the salt; this raise another problem of locating the samples in a beaker, which was not successful except for one sample out of the five which this method was attempted on. A final method attempted was to use a needle to scratch off the salt while submerged in deionised water; this proved successful in removing the salt, but also damaged the samples beyond recognition. A different insulator could potentially be used that would eliminate some of these issues, for example a salt that will dissolve more readily after being pressurised.

In future attempts to overcome these issues it may be better to make a transmitted light map of the sample, with markings on the surface, before loading into the FIB so that the heating spot can be located using the map. This may work on its own but it will also take a long time to cut through the salt using the FIB, so it may be necessary to either fully or partially polish the salt layer down before making the map. A better solution would be to pre-ablate most of the salt form the sample with a laser ablation system before finishing the sample lift out process with the FIB.

4.5.2 Evaluating the reliability of the results

There are a several reasons to be concerned about the accuracy of the diffusion coefficients measured in this study. The main reason for concern is that only one experiment was successfully processed using the FIB and then analysed, and with there being no other iron self-diffusion experiments conducted at such high pressure there is no way to tell whether this particular experiment has a significant error involved. The pressure reading for the sample is robust, although the temperature readings could be improved upon, as the temperature readings are an average, and the sample did experience variation within error from the temperatures reported here. The 2000 k diffusion measurement is more questionable, as it was estimated based on a series of coloured temperature maps, due to this the real error is likely greater than the error given by the error maps. The calculation of the diffusion coefficients appears reliable, although one of the assumptions within the calculation was that the diffusion couple is supposed to be effectively infinite and that diffusion is not supposed to pass to the end of either of the diffusion couples (Yunker and Van Orman, 2007). This assumption was not met in this study, as one of the major drawbacks of the diamond anvil cell is the size of the sample, and in this case the ^{57}Fe layer was so thin that diffusion did extend to the end of the layer. Overall the results from this study appear good, although the only way to be sure there are no significant errors would be to conduct more experiments at similar conditions to verify the results.

Another aspect regarding the reliability of the diffusion measurement is that in this study it could not be proven that the diffusion rate does not change with time. This is another limitation to only having one sample analysed, so that it cannot be determined whether there is any bias in the analysis methods or non-diffusive transport of material occurring. This could have been solved by analysing a range of samples with different experiment run times, which was originally a goal for this study.

4.5.3 Possible improvements

There are some improvements which could be made to the experiment design which might improve the reliability of the results and the likelihood of successfully extracting a sample using the focused ion beam. The iron foil which the samples were made from might be easier to work with and harder to damage if was thicker, a 10 µm thick iron foil would still easily fit into the sample

chamber in the DAC. The ^{57}Fe coating technique could also be made better by using more modern coating equipment, which would give a better indication of the thickness of the layer and potentially give a more even coat; although given that only one sample was successfully analysed the evenness of the ^{57}Fe is not known.

These recommendations should help to improve the reliability of sample extraction, however conducting more experiments would be the most reliable way to make sure more samples are successfully analysed. Once more experiments have been analysed it will then be possible to start improving and refining equation 8 and the model in figure 4.3b which it was used to generate.

4.5.4 Future directions for diamond anvil cell diffusion studies

The first step that should be taken is to build on this study by conducting more experiments in iron self-diffusion; in particular it would be useful to obtain some diffusivity measurements in the hcp phase, as it is the hcp phase which is most likely to exist in the Earth's lower mantle and core. Looking further ahead, this study provides a basis for conducting diffusion experiments using diamond anvil cells in any solid system under mantle conditions. While it would be possible to look at almost any system, perhaps the most relevant system for looking at planetary core formation would be the iron-nickel diffusion system, it would also be worth investigating a range of diffusion systems involving iron, nickel, silicon and sulphur.

5. Conclusions

This study has successfully measured the self-diffusion coefficient of fcc iron under 43.6 GPa, which is 20 GPa higher than the next comparable experiment; the diffusion coefficient was found to be two orders of magnitude faster than predicted by any of the existing models. While the goal of measuring the diffusion coefficient of iron under hcp conditions was not met, it is well within the capabilities of the methods outlined in this thesis to achieve these conditions.

At higher pressures it was found that T_m was no longer provided a reasonable approximation of pressure, and lead to the underestimation of diffusion coefficients in iron. The model created using equation 1 was recalculated using updated V^* (1.43 cm^3/mol) and E^* (431 kJ/mol) values from this study; this model now accurately predicts the diffusion coefficient in iron at high temperatures and pressures.

This study provides an experimental basis for further diffusion experiments using diamond anvil cells. Using this method, it is possible to simulate the diffusion conditions lower mantle, including measuring the diffusion of hcp iron. The methods outlined in this paper can easily be applied to the study of elemental self-diffusion, iron-nickel diffusion, and many other solid diffusion systems. The diffusion coefficients from such experiments can be applied to the study of the dynamics of the Earth's mantle, and the cores of smaller planets within the solar system.

References

Allègre, C. J., Poirier, J.-P., Humler, E., and Hofmann, A. W., 1995, The chemical composition of the Earth: Earth and Planetary Science Letters, v. 134, no. 3-4, p. 515-526.

Anzellini, S., Dewaele, A., Mezouar, M., Loubeyre, P., and Morard, G., 2013, Melting of Iron at Earth's Inner Core Boundary Based on Fast X-ray Diffraction: Science, v. 340, no. 6131, p. 464-466.

Badro, J., Côté, A. S., and Brodholt, J. P., 2014, A seismologically consistent compositional model of Earth's core: Proceedings of the National Academy of Sciences, v. 111, no. 21, p. 7542-7545.

Belonoshko, A. B., Lukinov, T., Fu, J., Zhao, J., Davis, S., and Simak, S. I., 2017, Stabilization of body-centred cubic iron under inner-core conditions: Nature Geoscience, v. 10, no. 4, p. 312-316.

Berg, M. T., Bromiley, G. D., Butler, I. B., Frost, M., Bradley, R., Carr, J., Le Godec, Y., Montési, L. G., Zhu, W., and Miller, K., 2017, Deformation-aided segregation of Fe-S liquid from olivine under deep Earth conditions: Implications for core formation in the early solar system: Physics of the Earth and Planetary Interiors, v. 263, p. 38-54.

Bouhifd, M., Clesi, V., Boujibar, A., Bolfan-Casanova, N., Cartier, C., Hammouda, T., Boyet, M., Manthilake, G., Monteux, J., and Andrault, D., 2017, Silicate melts during Earth's core formation: Chemical Geology, v. 461, p. 128-139.

Campbell, A. J., 2008, Measurement of temperature distributions across laser heated samples by multispectral imaging radiometry: Review of Scientific Instruments, v. 79, no. 1, p. 015108.

Canup, R. M., 2012, Forming a Moon with an Earth-like composition via a giant impact: Science, v. 338, no. 6110, p. 1052-1055.

Chambers, J. E., 2004, Planetary accretion in the inner Solar System: Earth and Planetary Science Letters, v. 223, no. 3, p. 241-252.

Ćuk, M., and Stewart, S. T., 2012, Making the Moon from a fast-spinning Earth: a giant impact followed by resonant despinning: science, v. 338, no. 6110, p. 1047-1052.

Deguen, R., 2012, Structure and dynamics of Earth's inner core: Earth and Planetary Science Letters, v. 333, p. 211-225.

Dobson, D. P., 2002, Self-diffusion in liquid Fe at high pressure: Physics of the Earth and Planetary Interiors, v. 130, no. 3, p. 271-284.

Dobson, D. P., and Wiedenbeck, M., 2002, Fe-and C-self-diffusion in liquid Fe3C to 15 GPa: Geophysical research letters, v. 29, no. 21.

Dorogokupets, P., Dymshits, A., Litasov, K., and Sokolova, T., 2017, Thermodynamics and Equations of State of Iron to 350 GPa and 6000 K: Scientific Reports, v. 7.

Dumberry, M., and Rivoldini, A., 2015, Mercury's inner core size and core-crystallization regime: Icarus, v. 248, no. Supplement C, p. 254-268.

Fischer, R. A., Campbell, A. J., and Ciesla, F. J., 2017, Sensitivities of Earth's core and mantle compositions to accretion and differentiation processes: Earth and Planetary Science Letters, v. 458, p. 252-262.

Goldstein, J., Hanneman, R., and Ogilvie, R., 1965, Diffusion in the fe-ni system at 1 atm and 40 kbar pressure(Interdiffusion coefficients for Fe-Ni alloy as function of composition in alpha and gamma phases at 1 atm and 40 kbar pressure): AIME, TRANSACTIONS, v. 233, p. 812-820.

Gordon, R., 1967, Diffusion creep in the Earth's mantle: Jour. Geophys. Research, v. 70.

Heumann, T., and Imm, R., 1968, Self-diffusion and isotope effect in γ-iron: Journal of Physics and Chemistry of Solids, v. 29, no. 9, p. 1613-1621.

Ito, E., 2007, Theory and practice—multianvil cells and high-pressure experimental methods: Treatise on geophysics, v. 2, p. 197-230.

James, D., and Leak, G., 1966, Self-diffusion and diffusion of cobalt in alpha and delta-iron: Philosophical Magazine, v. 14, no. 130, p. 701-713.
Kaminski, E., and Javoy, M., 2013, A two-stage scenario for the formation of the Earth's mantle and core: Earth and Planetary Science Letters, v. 365, p. 97-107.
Kavner, A., Duffy, T. S., and Shen, G., 2001, Phase stability and density of FeS at high pressures and temperatures: implications for the interior structure of Mars: Earth and Planetary Science Letters, v. 185, no. 1, p. 25-33.
Komabayashi, T., and Fei, Y., 2010, Internally consistent thermodynamic database for iron to the Earth's core conditions: Journal of Geophysical Research: Solid Earth, v. 115, no. B3, p. n/a-n/a.
Konôpková, Z., McWilliams, R. S., Gómez-Pérez, N., and Goncharov, A. F., 2016, Direct measurement of thermal conductivity in solid iron at planetary core conditions: Nature, v. 534, no. 7605, p. 99-101.
Malavergne, V., Toplis, M. J., Berthet, S., and Jones, J., 2010, Highly reducing conditions during core formation on Mercury: Implications for internal structure and the origin of a magnetic field: Icarus, v. 206, no. 1, p. 199-209.
Mann, U., Frost, D. J., and Rubie, D. C., 2009, Evidence for high-pressure core-mantle differentiation from the metal–silicate partitioning of lithophile and weakly-siderophile elements: Geochimica et Cosmochimica Acta, v. 73, no. 24, p. 7360-7386.
Mao, W. L., Campbell, A. J., Heinz, D. L., and Shen, G., 2006, Phase relations of Fe–Ni alloys at high pressure and temperature: Physics of the Earth and Planetary Interiors, v. 155, no. 1, p. 146-151.
McDonough, W. F., and Sun, S.-S., 1995, The composition of the Earth: Chemical geology, v. 120, no. 3-4, p. 223-253.
Reaman, D. M., Colijn, H. O., Yang, F., Hauser, A. J., and Panero, W. R., 2012, Interdiffusion of Earth's core materials to 65GPa and 2200K: Earth and Planetary Science Letters, v. 349, p. 8-14.
Righter, K., Pando, K., Danielson, L., and Lee, C.-T., 2010, Partitioning of Mo, P and other siderophile elements (Cu, Ga, Sn, Ni, Co, Cr, Mn, V, and W) between metal and silicate melt as a function of temperature and silicate melt composition: Earth and Planetary Science Letters, v. 291, no. 1, p. 1-9.
Rubie, D. C., Frost, D. J., Mann, U., Asahara, Y., Nimmo, F., Tsuno, K., Kegler, P., Holzheid, A., and Palme, H., 2011, Heterogeneous accretion, composition and core–mantle differentiation of the Earth: Earth and Planetary Science Letters, v. 301, no. 1, p. 31-42.
Rubie, D. C., Jacobson, S. A., Morbidelli, A., O'Brien, D. P., Young, E. D., de Vries, J., Nimmo, F., Palme, H., and Frost, D., 2015, Accretion and differentiation of the terrestrial planets with implications for the compositions of early-formed Solar System bodies and accretion of water: Icarus, v. 248, p. 89-108.
Sammis, C. G., Smith, J. C., and Schubert, G., 1981, A critical assessment of estimation methods for activation volume: Journal of Geophysical Research: Solid Earth, v. 86, no. B11, p. 10707-10718.
Siebert, J., Corgne, A., and Ryerson, F. J., 2011, Systematics of metal–silicate partitioning for many siderophile elements applied to Earth's core formation: Geochimica et Cosmochimica Acta, v. 75, no. 6, p. 1451-1489.
Stewart, A. J., Schmidt, M. W., van Westrenen, W., and Liebske, C., 2007, Mars: A New Core-Crystallization Regime: Science, v. 316, no. 5829, p. 1323-1325.
Swartzendruber, L., Itkin, V., and Alcock, C., 1991, The Fe-Ni (iron-nickel) system: Journal of phase equilibria, v. 12, no. 3, p. 288-312.
Tateno, S., Hirose, K., Ohishi, Y., and Tatsumi, Y., 2010, The Structure of Iron in Earth's Inner Core: Science, v. 330, no. 6002, p. 359-361.

Uchida, T., Wang, Y., Rivers, M. L., and Sutton, S. R., 2001, Stability field and thermal equation of state of ε-iron determined by synchrotron X-ray diffraction in a multianvil apparatus: Journal of Geophysical Research: Solid Earth, v. 106, no. B10, p. 21799-21810.

Walter, C. M., and Peterson, N., 1969, Isotope effect in self-diffusion in iron: Physical Review, v. 178, no. 3, p. 922.

Walter, M. J., and Cottrell, E., 2013, Assessing uncertainty in geochemical models for core formation in Earth: Earth and Planetary Science Letters, v. 365, p. 165-176.

Watson, E. B., and Baxter, E. F., 2007, Diffusion in solid-Earth systems: Earth and Planetary Science Letters, v. 253, no. 3, p. 307-327.

Wood, B. J., and Halliday, A. N., 2005, Cooling of the Earth and core formation after the giant impact: Nature, v. 437, no. 7063, p. 1345.

Wood, B. J., Walter, M. J., and Wade, J., 2006, Accretion of the Earth and segregation of its core: Nature, v. 441, no. 7095, p. 825.

Yang, J., and Goldstein, J., 2004, Magnetic contribution to the interdiffusion coefficients in bcc (α) and fcc (γ) Fe-Ni alloys: Metallurgical and Materials Transactions A, v. 35, no. 6, p. 1681-1690.

Yin, Q., Jacobsen, S., Yamashita, K., Blichert-Toft, J., Télouk, P., and Albarede, F., 2002, A short timescale for terrestrial planet formation from Hf-W chronometry of meteorites: Nature, v. 418, no. 6901, p. 949.

Yoshino, T., 2010, Laboratory electrical conductivity measurement of mantle minerals: Surveys in Geophysics, v. 31, no. 2, p. 163-206.

Yu, G., and Jacobsen, S. B., 2011, Fast accretion of the Earth with a late Moon-forming giant impact: Proceedings of the National Academy of Sciences, v. 108, no. 43, p. 17604-17609.

Yunker, M. L., and Van Orman, J. A., 2007, Interdiffusion of solid iron and nickel at high pressure: Earth and Planetary Science Letters, v. 254, no. 1, p. 203-213.

Zhang, B., 2014, Calculation of self-diffusion coefficients in iron: AIP Advances, v. 4, no. 1, p. 017128.

Software

Benson, D. Poczatek, C., Epstein, B., Gormanns, P., Reckow, S., Gonzales, R., Kaufman, Z., 2017. OpenMIMS, Harvard, https://github.com/BWHCNI/OpenMIMS; http://www.nrims.hms.harvard.edu/

Oliver T. Lord, 2017. Black V5, University of Bristol.

Oliver T. Lord, 2017. 4color, University of Bristol.